Universidad de Concepción

Universidad de Concepción

The formation of dwarf spheroidal galaxies including their star formation histories

(La formación de galaxias esferoidales enanas incluyendo sus historias de formación estelar)

Tesis para ser presentada en la dirección de postgrado de la Universidad de Concepción para optar al grado de

Magister en ciencias con mención en física

Alex Rodrigo Alarcón Jara

Asesor: Dr. Michael Fellhauer

Concepción, Chile
Junio 2017

Agradecimientos

Quisiera dar las gracias a todas las personas que me acompañaron durante mis años de estudio, en especial a las que me ayudaron a hacer este trabajo.

Primero doy gracias a mis amigos y compañeros de carrera con los que codo a codo estuvimos luchando juntos para terminar la carrera universitaria, un agradecimiento especial a los que llegamos juntos hasta el final, ellos son Lientur Celedon, Pedro Humire, Gerald Neumann, Bastian Reinoso y Diego Matus, ellos han sido un apoyo fundamental desde el inicio de mis estudios universitarios.

Doy gracias a mi familia, por su apoyo incondicional tanto ecónomico como emocional, en especial a mis padres José Alarcón y Patricia Jara que lo han dado todo para que yo pueda salir adelante con mis estudios universitarios de pregrado y postgrado, sin ellos no hubiera sido posible hacer todo lo que he logrado académicamente.

Doy gracias a mi tutor Michaell Fellhauer a Paulina Assmann y a los demas miembros del Theory and Star Formation Group in Concepción por la paciencia y la buena disposición de responder todas las dudas que surgían durante mi trabajo en esta tesis.

Finalmente quiero dar las gracias a Dominik Schleicher, a la Universidad de Concepción y a Dirección de Postgrado por la ayuda financiera, ya que fue muy útil para asistir a escuelas y congresos para aprender de otros temas y exponer acerca de este trabajo en otros centros de investigación.

Abstract

Dwarf spheroidal (dSph) galaxies are regarded as the basic building blocks in the formation of larger galaxies and are believed to be the most dark matter dominated systems known in the Universe. There are several models that attempt to explain their formation and evolution, but they have problems to model the formation of isolated dSph galaxies. Here we will explain a possible formation scenario in which star clusters form inside the dark matter (DM) halo of a dSph. Those star clusters suffer from low star formation efficiency and dissolve while orbiting inside the DM halo. Thereby they build the faint luminous components that we observe in dSph galaxies. In this thesis we study this model by adding different star formation histories to the simulations to compare the results with previous works and observational data to show that we can explain the formation of dSph galaxies.

Resumen

Las galaxias enanas esferoidales son reconocidas como el bloque básico de construcción de galaxias mas grandes y se cree que son los sistemas mas dominados por materia oscura conocidos en el Universo. Hay algunos modelos que intentan explicar su formación y evolución, pero tienen problemas para modelar la formación de galaxias esferoidales enanas aisladas. Aquí explicaremos un posible escenario de formación en el cual cúmulos de estrellas se forman dentro del halo de materia oscura de una galaxia esferoidal enana. Estos cumulos de estrellas tienen baja eficiencia de formación estelar y se disuelven mientras orbitan dentro del halo de materia oscura. Así ellos construyen la débil componente luminosa que observamos en galaxias esferoidales enanas. En esta tesis estudiaremos este modelo añadiendo diferentes historias de formación estelar a las simulaciones para comparar los resultados con trabajos previos y datos observacionales para mostrar que podemos explicar la formación de galaxias enanas esferoidales.

Contents

List of Figures

List of Tables

Chapter 1

Introduction

1.1 Dwarf galaxies in the Local Group

The Local Group (LG) is a collection of gravitationally bound galaxies, some of the characteristics of this group are mentioned in van den Bergh et al. (1999), where they reported a radius for our Local Group of about $R_{LG} = 350$ kpc, a total mass and luminosity of $M_{LG} = 2.3 \pm 0.6 \times 10^{12}\, M_\odot$ and $M_v = -22$ mag respectively, this implies a mass to light ratio of $M/L=(44 \pm 12)\ M_\odot/L_\odot$, with a velocity dispersion $\sigma = (61 \pm 8)$ km/s. In Figure 1.1 we can see how the galaxies are distributed in the Local Group.

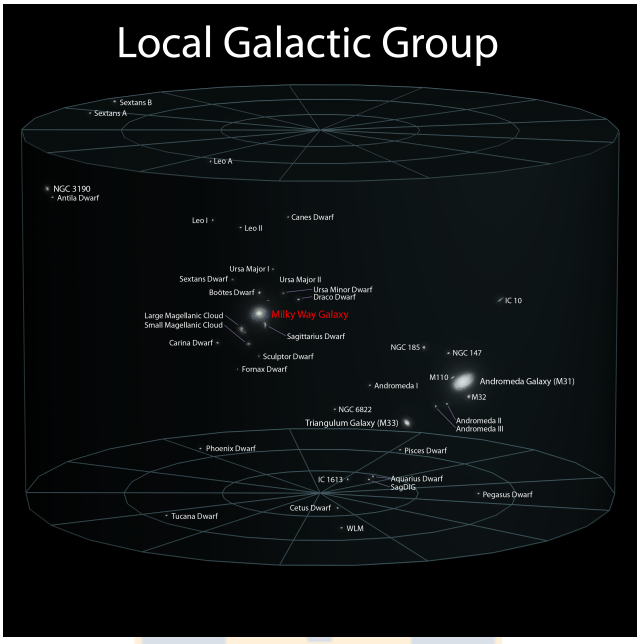

Figure 1.1: Distribution of the galaxies inside the Local Group (LG), credits Andrew Z. Colvin.

The Local Group has more than 80 galaxies, reported by Mconachie 2012, this number has grown significantly in the last years due to the observations of the Sloan Digital Sky Survey (SDSS)(York et al., 2000) and similar surveys like DES (Flaugher, 2005) and PANstars (Kaiser et al., 2002), most of the galaxies in the Local Group are dwarf galaxies orbiting the three largest galaxies of the group: the Milky Way (MW), the Andromeda galaxy and the Triangulum galaxy (M33), also we see isolated dwarf galaxies that are far away from the biggest galaxies. In the Table 1.1 we can see the properties of some known dwarf galaxies.

The main distingishly feature to call a galaxy a dwarf is its mass. All galaxies with less than $10^{10}M_{\odot}$ are considered to be dwarf galaxies.

The main importance of the dwarf galaxies is that, according to the cosmological model Lambda Cold Dark Matter (Λ-CDM), they are the basic building blocks of bigger galaxies through major and/or minor

Table 1.1: Properties of some dwarf galaxies of the LG (Weisz et al., 2014), physical properties taken from Mconachie (2012), the stellar mass listed in column (4) is computed for the integrated V-band luminosity and assumes M./L. = 1

Galaxy Name (1)	Morphological Type (2)	$(m-M)_o$ (3)	A_v (mag) (4)	M_v (5)	M_* (10^6 M.) (6)	M_{HI} (10^6 M.) (7)	Distance to Nearest Host (kpc) (8)	r_h (pc) (9)
Andromeda I	dSph	24.36± 0.07	0.15	-11.7	3.9	0.0	58	672
Andromeda II	dSph	24.07± 0.06	0.17	-12.4	7.6	0.0	184	1176
Andromeda III	dSph	24.37 ± 0.07	0.15	-10.0	0.83	0.0	75	479
Andromeda V	dSph	24.44 ± 0.08	0.34	-9.1	0.39	0.0	110	315
Andromeda VI	dSph	24.47 ± 0.07	0.17	-11.3	2.8	0.0	269	524
Andromeda VII	dSph	24.41 ± 0.10	0.53	-12.6	9.5	0.0	218	776
Andromeda XI	dSph	$24.40^{+0.2}_{-0.5}$	0.21	-6.9	0.049	0.0	104	157
Andromeda XII	dSph	24.47± 0.30	0.30	-6.4	0.031	0.0	133	304
Andromeda XIII	dSph	$24.80^{+0.1}_{-0.4}$	0.23	-6.7	0.041	0.0	180	207
Carina	dSph	20.11 ± 0.13	0.17	-9.1	0.38	0.0	107	250
Cetus	dSph	24.38 ± 0.07	0.08	-11.2	2.6	0.0	756	703
Canes Venatici I	dSph	21.69 ± 0.10	0.04	-8.6	0.23	0.0	218	564
Canes Venatici II	dSph	21.02 ± 0.06	0.03	-4.9	0.0079	0.0	161	74
DDO 210	dTrans	25.15 ± 0.08	0.14	-10.6	1.6	4.1	1066	458
Draco	dSph	19.40 ± 0.17	0.07	-8.8	0.29	0.0	76	221
Fornax	dSph	20.84± 0.18	0.06	-13.4	20.0	0.0	149	710
Hercules	dSph	20.60 ± 0.20	0.17	-6.6	0.037	0.0	126	330
IC 10	dIrr	24.50± 0.12	4.3	-15.0	86.0	50.0	252	612
IC 1613	dIrr	24.39 ± 0.12	0.07	-15.2	100.0	65.0	520	1496
Leo A	dIrr	24.51 ± 0.12	0.06	-12.1	6.0	11.0	803	499
Leo I	dSph	22.02 ± 0.13	0.10	-12.0	5.5	0.0	258	251
Leo II	dSph	21.84 ± 0.13	0.05	-9.8	0.74	0.0	236	176
Leo IV	dSph	20.94 ± 0.09	0.07	-5.8	0.019	0.0	155	206
Leo T	dTrans	23.10 ± 0.10	0.09	-8.0	0.14	0.28	422	120
LGS 3	dTrans	24.42 ± 0.07	0.11	-10.1	0.96	0.38	269	470
M32	dE	24.53 ± 0.21	0.17	-16.4	320.0	0.0	23	110
NGC 147	dE	24.15 ± 0.09	0.47	-14.6	62.0	0.0	142	623
NGC 185	dE	23.95 ± 0.09	0.50	-14.8	68.0	0.11	187	42
NGC 205	dE	24.58 ± 0.07	0.17	-16.5	330.0	0.4	42	590
NGC 6822	dIrr	23.31 ± 0.08	0.65	-15.2	100.0	130.0	452	354
Pegasus	dTrans	24.82 ± 0.07	0.19	-12.2	6.61	5.9	474	562
Phoenix	dTrans	23.09 ± 0.10	0.04	-9.9	0.77	0.12	415	454
Sag DIG	dIrr	25.14 ± 0.18	0.34	-11.5	3.5	8.8	1059	282
Sagittarius	dSph	17.10 ± 0.15	0.42	-13.5	21.0	0.0	18	2587
Sculptor	dSph	19.67 ± 0.14	0.05	-11.1	2.3	0.0	89	283
Sex A	dIrr	25.78 ± 0.08	0.12	-14.3	44.0	77.0	1435	1029
Sex B	dIrr	25.77 ± 0.03	0.09	-14.4	52.0	51.0	1430	440
Tucana	dSph	24.74± 0.12	0.09	-9.5	0.56	0.0	882	284
Ursa Minor	dSph	19.40 ± 0.10	0.09	-8.8	0.29	0.0	78	181
WLM	dIrr	24.85 ± 0.08	0.10	-14.2	43.0	61.0	836	2111

mergers (e.g Kauffmann et al. 1993; Cole et al. 1994), so we need to study them to understand the process of formation and evolution of the biggest galaxies and the Universe as a whole.

1.2 Classification of dwarf galaxies

Dwarf galaxies can be classified in three major types, dwarf irregular (dIrr), dwarf elliptical (dE) and dwarf spheroidal galaxies (dSph). Now we will briefly summarize some of the properties of the different types of dwarf galaxies.

1.2.1 Dwarf Irregular (dIrr)

They have a high star formation rate and are rich in neutral hydrogen, between the 20 % to 50 % of its total mass is in form of this gas, its irregular form is given by the distribution of its gas and the blue stars which are distributed irregularly in the galaxy, while the red stars are distributed forming a disk, the best known example for a dIrr galaxy is the Large Magellanic Cloud (LMC).

1.2.2 Dwarf Elliptical (dE)

They have absolute magnitudes within the range $-18 <$M< -14, they do not have significative quantities of gas and are very compact, the common diameters are between 1 to 10 kpc (Caldwell 1995). It is believed that its elliptical form is given by tidal forces with other galaxies. Also we can subclassify this type of galaxy depending on if they have a nuclei or not.

1.2.3 Dwarf Spheroidal (dSph)

They are the dominant population in the Local Group, they are almost without of gas and most of them have an old stellar population and are devoid of gas or dust. They have high velocity dispersion ranging between 5 and 12 km/s and have very low luminosities, $M_v \approx -11$ (Mateo, 1998). Analyzing the velocity distribution of their stars we

can conclude that they are dark matter dominated (Lokas, 2008; Lokas, 2011).

1.3 Large Λ-CDM simulations

In the frame of the Λ-CDM model, dwarf galaxies are the basic building blocks of bigger structures (Kauffmann et al. 1993; Cole et al. 1994). There are studies made with large N-body simulation following this model to study the formation and evolution of the Universe, for example the Millennium Simulation (Springel V. et.al 2005, Figure 1.2) and the Milky Way Simulation (Diemand J. et al. 2008, Figure 1.3).

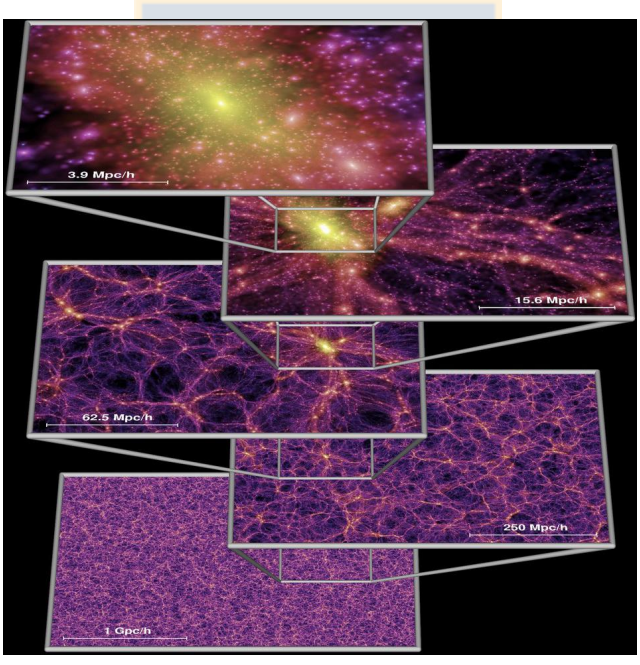

Figure 1.2: The Millennium Simulation: This picture shows the dark matter distribution in the Universe at the present time, based on the Millennium simulation it is one of the largest N-body simulation carried out so far (more than 10^{10} particles.)

These N-body simulations show that DM haloes naturally form over time, and these haloes have cusped shapes described by a Navarro, Frenk & White (NFW) profile (Navarro et al 1997). The NFW model is fitted by the formula:

$$\rho_{NFW} = \frac{\rho_0}{(\frac{r}{r_s})(1+\frac{r}{r_s})^2} = \frac{\delta_{\rm char}\rho_c}{(\frac{r}{r_s})(1+\frac{r}{r_s})^2} \tag{1.1}$$

where $\rho_c = 3H_0^2/8\pi G$ is the critical density of the Universe. The parameter r_s is a characteristic radius, $\delta_{\rm char}$ is the characteristic overdensity. $\delta_{\rm char}$ is a dimensionless parameter. This profile is truncated at the virial radius, r_{200}. It represents the radius within which the mean density is $200 \times \rho_c$, and it is defined by the following expression

$$r_{200} = r_s c \tag{1.2}$$

where c is the concentration parameter. δ_{char} and c are related by

$$\delta_{char} = \frac{200c^3}{3(ln(1+c) - \frac{c}{1+c})} \tag{1.3}$$

The problem of these simulations is that, according to observations, the density profiles of the DM haloes have cored shapes and may be similar to a Plummer sphere distribution (Plummer et. al 1911).

$$\rho_{pl} = \left(\frac{3M}{4\pi a^3}\right)\left(1+\frac{r^2}{a^2}\right)^{\frac{-5}{2}} \tag{1.4}$$

Where M is the total mass and a is the Plummer radius.
The possible solutions to this problem could be:

a) DM halos must have cusped distributions, so the stated limits hold and provide new constraints on cosmological parameters (Valenzuela et.al 2007).

b) Something (e.g. feedback, modifications of the nature of dark matter) eliminates cusps and thus the constraints on cosmology (Governato et.al 2010).

c) The picture of halo formation suggested by Λ-CDM simulations is wrong

Another prediction of these simulations is that a galaxy like the Milky Way has to be surrounded by one hundred to one thousand of DM halos that could host a dwarf galaxy. At the present we have discovered more than 30 of these satellites orbiting the Milky Way. This big difference between the number of galaxies predicted and observed is called Missing Satellites Problem (Klypin et.al 1999).

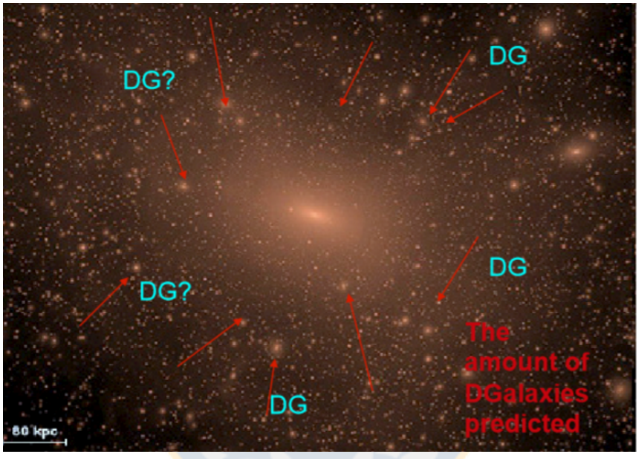

Figure 1.3: The Via Lactea Simulation. Projected DM density square maps of the simulated Milky Way-size halo at redshift z = 0.The arrows indicate the DM haloes of dwarf galaxies around a Milky Way-size halo. Credit J. Diemand and P. Assmann.

A possible explanation is found in (Koposov S.E. et.al 2009), where they combine a dynamical model for the DM sub-halo populations. In this work they consider a suppression of star formation "before" reionization in halos with circular velocities less than 35 km/s. This scenario explains quantitatively the observed satellites in the MW, however, the model does not explain why observations indicate that DM haloes of the dwarf galaxies rather show a cored profile, since they predict that DM haloes have a cusped NFW profile.

In order to try to give a solution to the Missing Satellites Problem we have to understand how the dwarf galaxies were formed, especially the dSph galaxies which are the most abundant population in the Local Group.

1.4 Formation of dwarf spheroidal galaxies

Nobody know exactly how the dSph were formed, but there are several models which attempt to explain their properties and characteristics using different mechanism. Now we will briefly summarize some of them.

1.4.1 The Tidal Stirring and Ram pressure stripping model

In (Gnedin, Hernquist & Ostriker 1999; Mayer et al. 2007) the authors propose that dSph galaxies were formed from dwarf disc satellites orbiting a mayor galaxy. Their gas is removed by ram-pressure and additional tidal stirring changed their form. This model predicts that the biggest galaxies should be surrounded by dwarf galaxies dominated by DM.

1.4.2 Resonant Stripping model

In this model the authors (D'Onghia et al. 2009) propose that dSph galaxies were formed by encounters between two dwarf disc galaxies, and resonant stripping destroyed the form of the galaxies, letting their DM halo intact. Then the stars regroup inside the potentials of the DM haloes, forming two dSph galaxies. This model can explain the kinematic and morphology of some known dSph galaxies and also predicts that the shocks should produce long stellar streams and tails.

One of the disadvantage of these models are that we need interactions between two or more galaxies to explain dSphs, so we can not use them to explain the formation of isolated dSph galaxies.

1.4.3 Sawala isolated models

In the work of Sawala et al. (2010) they perform cosmological zoom-in simulations of dwarf haloes in the mass range 2.3×10^8 to 1.1×10^9 $M_\odot$

using a SPH code with a star formation recipe. Where the density of the gas is sufficiently high, they convert gas particles into star particles, having masses of about 10^2 to 10^3 $M_\odot$. They do not take into account, that those masses in stars would form in an association or in a small dissolving cluster, because it is below their resolution, nor that more massive star clusters could form in a single star forming event.

The dissolving star cluster model, which we will summarize in the next subsection, can explain the formation of this isolated dSph galaxies, because it does not need another galaxy to explain the formation of a dSph galaxy.

1.5 Dissolving star clusters model

This thesis is based on the study of this model proposed by Assmann et al. 2013. According to this model a dSph galaxy is formed by the fusion and dissolution of several star cluster formed in giants gas clouds within a dark matter halo, and after 10 Gyr of evolution we have a dSph galaxy, a simple representation of this model is shown in Figure 1.4.

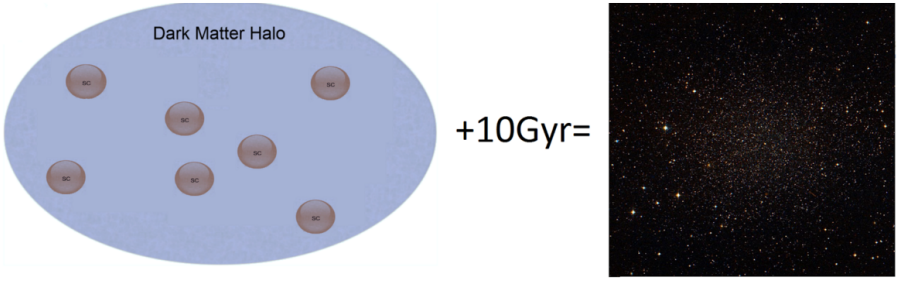

Figure 1.4: A simple representation of dissolving star cluster model, the star clusters formed in a dark matter halo evolve and mix with each other and form a dSph galaxy after 10 Gyr.

This model can explain how we form dSph galaxies, their kinematics and morphologies even the properties of isolated dSph galaxies. This model is based in two widely accepted theories, the cosmological model

Λ-CDM and the formation of star cluster.

1.6 Basis of the dissolving star clusters model

1.6.1 Lambda CDM cosmological model

The Λ-CDM model proposes that galaxies form in DM haloes. In this model the biggest haloes are formed through the merging of small haloes in a process driven by gravitational forces. The small DM haloes are produced due to the fluctuations of the primordial density field (Figure 1.5). The smallest haloes which are able to retain gas and form stars are the haloes of dwarf galaxies.

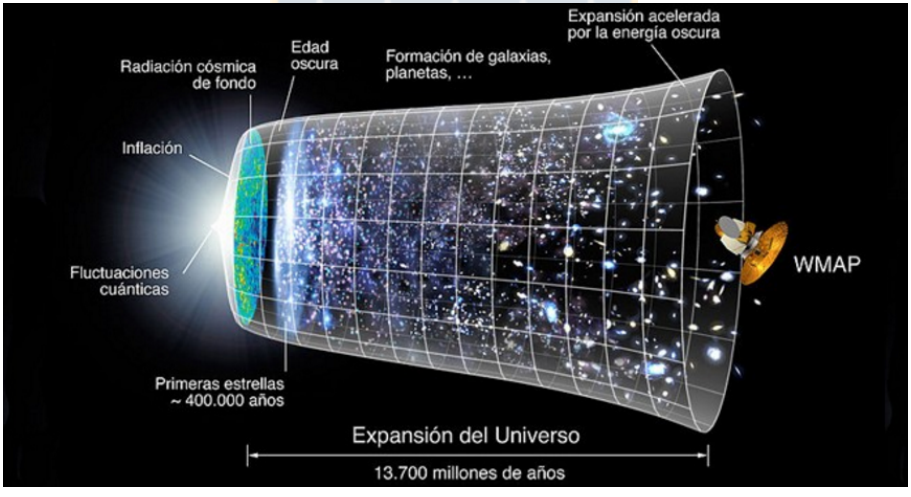

Figure 1.5: A representation of the evolution of the Universe over 13.7 billion years. In the earliest moment that we can now probe, the Universe grew up exponentially. Due to gravity, the expansion of the Universe gradually slowed down. Afterwards, the universal expansion started to accelerate again as the repulsive effects of dark energy became relevant. Credit: NASA / WMAP Science Team.

This model is widely accepted because is in concordance with the Big

Bang, CMB (Spergel D. N et al. 2993), the structure of the Universe at large scales and observations of supernovas (Hamuy et al. 1996, Perlmutter et al. 1999 and Riess et al. 2004), and it is now widely accepted that the Universe is flat, with the cosmological parameters approximately given by: the Hubble constant H_0=h100km/s/Mpc with h=0.72, the baryonic mass fraction $\omega_b h^2 = 0.0227$ and the total mass fraction $\omega_m h^2 = 0.133$ (Lada et al. 2003).

The Λ-CDM model is based on the existence of the dark matter, a hypothetical matter which does not emit electromagnetic radiation, but we can deduce its existence by its gravitational effects it is causing in stars and galaxies.

1.6.2 Star cluster formation

The standard theories of star formation propose that stars form in clusters and never isolated, a star cluster is a group of stars gravitationally bound with stars having the same age and metallicity, such that the only variable parameter is their mass, they are an excellent laboratory to study the stellar formation process.

The stars of star clusters form from a giant molecular gas cloud mainly composed by molecular Hydrogen and dust with a temperature about 10K to 20K. When gravity wins over the pressure, the gas begins to collapse and to form cores. This process is called Jeans instability. The cores collapse further forming protostars. In the final step of the star cluster formation, stars have formed in the embedded cluster phase that means that they are still surrounded by gas, then the stars expel the remaining gas by radiation, stellar winds and supernovae leaving the star cluster out of virial equilibrium and expanding. If some stars have high velocities they can escape. According to the theory if the star formation efficiency is about 30% the star cluster survives (Lada & Lada 2003), if it is lower the star cluster dissolves completely, the star formation efficiency is defined as the rate between the mass of the stars and the mass of the gas and stars, it is useful to measure how many gas is transformed into stars, see Equation 1.5.

$$SFE = \frac{M_*}{M_* + M_{\rm gas}} \tag{1.5}$$

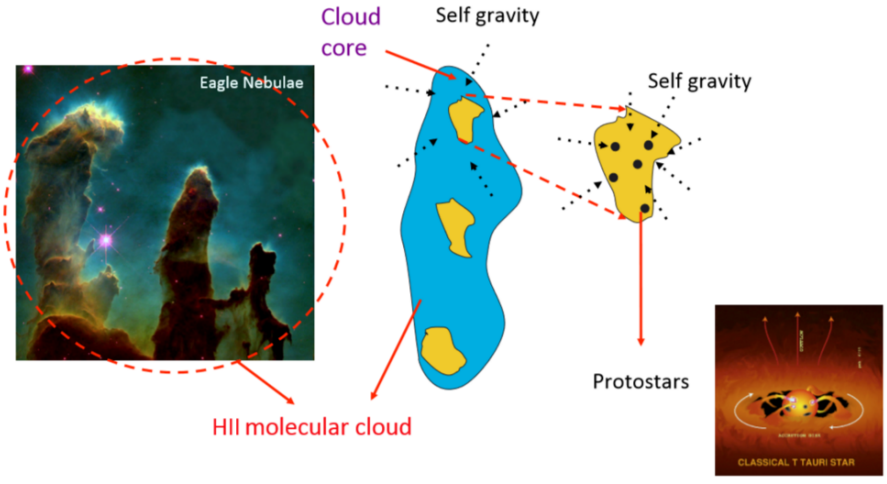

Figure 1.6: The process of star formation. This picture shows the steps of the formation of stars from a molecular gas cloud to a protostar. credit: P. Assmann.

1.7 Previous studies of dissolving star cluster models

Using the Λ-CDM and the star cluster formation theory to build the luminous component of the dSph galaxy, we have to consider that the gas inside a DM halo of a dSph might form many star clusters, these star clusters interact with each other and deposit stars in the center of the DM halo, at the same time they expand and dissolve and after ten Gyr we will get a dSph galaxy.

This model was studied before by Assmann et al. (2013a,b) In their work they made simulations with different numbers of star cluster N_0 = 15,30 and 60, keeping the total mass of the N star clusters, $M_{total} = 4.5 \times 10^5 M_\odot$, which is a typical total mass of the luminous component of classical dSph galaxies, they use different star formation efficiencies of SFE= 15%, 30% and 60%. Also they varied the distribution of the star cluster within the dark matter halo, as they do not

know exactly how are the N star cluster within the dark matter halo are distributed. The authors assume for simplicity a Plummer distribution because they expect that more star clusters form in the center than in the outer parts. In their simulations they varied the scale length of the Plummer distribution R_{SC}=0.25, 0.5, 1.0 kpc. Also they made simulations with two different dark matter halo profiles, using a cusped profile as predicted by Λ-CDM simulations which is fitted by a Navarro Frenk & White profile and with a cored profile as is predicted by observations using a Plummer distribution, with different masses of the DM halo within 500 pc, M_{500}=1 × 10^7, 4×10^7 , 1×10^8 $M_\odot$. A representation of their simulations is shown in (Figure 1.7), the set of parameters shown can resembles the properties of classical dSph and is called fiducial model.

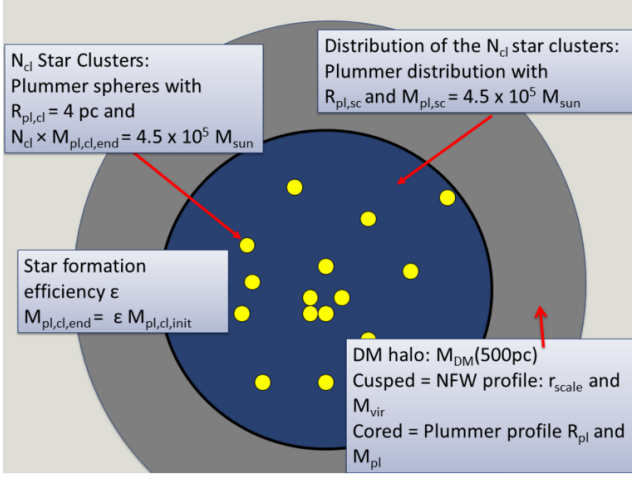

Figure 1.7: Setup of the previous work of Assmann et al. 2012 in which we see the different parameters that they used, this set of parameters can explain the properties of classical dSph and is called Fiducial model.

They simulate the SCs within the DM halo for 10 Gyr with different combinations of parameters and at the end of the simulation they analyze the kinematics and morphologies of the final objects and then compare the simulations with observational data of classical dSph

galaxies, concluding that the simulations can resemble some properties of classical dwarf spheroidal galaxies. (Figure 1.8 and 1.9)

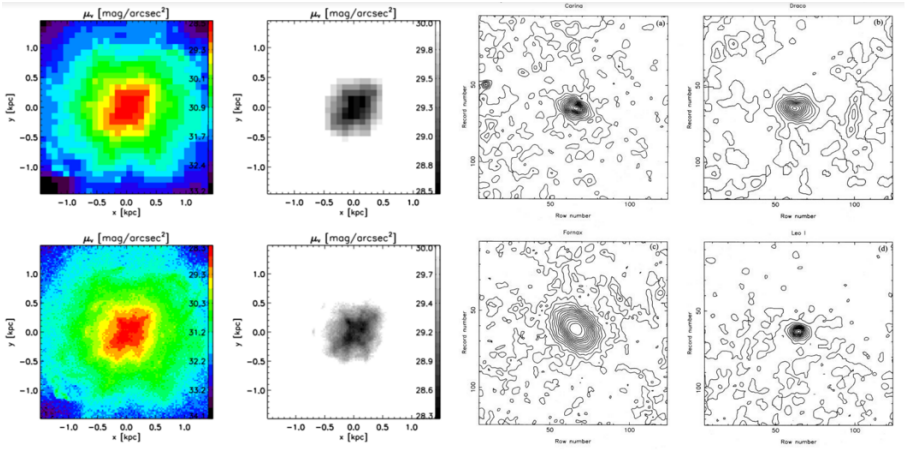

Figure 1.8: In the left side we see a final object of the simulations of Assmann et al. with high and low resolution and a cut at 30 mag/arcsec^2, in the right side, we see maps of densities of some classical dSph galaxies taken from Irwin 1995, we can see that the final objects of the simulations can resemble the morphologies of the classical dSph galaxies.

Some of their conclusion are:

- Using the parameters of the fiducial model the best fit for the surface brightness profile is a Sérsic profile with $\Sigma_{eff} = 0.115 \pm 0.003$ M$_\odot$/pc^2, $R_{eff} = 500 \pm 10$ pc and $n = 0.94 \pm 0.01$.
- Simulations provide profiles similar to dSph galaxies with exponential profiles.
- Larger halo scale-lengths give profiles with lower central densities, smaller scale lengths of the star cluster distribution give more concentrated objects.
- The surface brightness profiles do not depend on the enclosed halo mass.

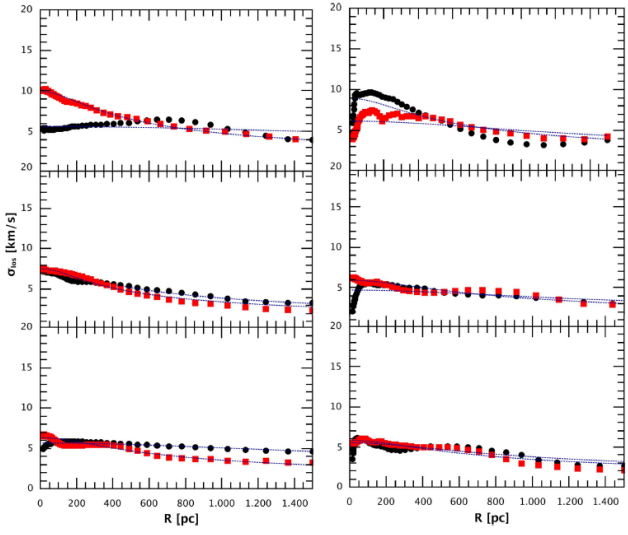

Figure 1.9: Velocity dispersion of some simulations did by Assmann et al., We see that the velocity dispersion is in the range of observed velocities of dwarf spheroidal galaxies which range between 5 to 12km/s, and this value is constant independent of the distance from the center.

- Velocity dispersions of their simulations are in the range that we can observe in the classical dSph galaxies which are between 5 and 12 km/s.
- Velocity dispersion depends only on the enclosed halo mass.
- There is no dependence on the initial number of star clusters on the final object.

In all these simulations the authors simulated a scenario in which the N star clusters form at the beginning of the simulations, but we know that the stars in dSph galaxies have different ages, that means they have star formation histories (SFH) In this thesis we will add SFH to the simulations to the fiducial model to study the differences between the work done by Assmann et al. (2013a,b) and compare the results

with observational data.

1.8 Star formation histories (SFH) in Dwarf galaxies

All known dwarf galaxies in the LG have been observed with space- and/or ground-based imaging. These data reveal the resolved stellar populations, allowing us to infer their stellar age distributions with the color-magnitud diagram (CDM) analyzing the stars on the main sequence as done by Weisz et al. 2014 with data from the HST.

Some of the results of Weisz et al. 2014 are shown in figure 1.10, the authors studied the SFH of classical dSph galaxies of the MW to show that the SFH of them varies between high starbursts where almost all the stars of the galaxy were formed at the same time until constant star formation histories, where the stars are formed constantly until today. Others dwarf galaxies show SFH with two burst in which they have a high star formation at the beginning, then nothing happens, and then again a high star burst happens, to form the stars of the galaxy, Tucana is an example of this kind of SFH.

In this thesis we will study the effect of the SFH in the fiducial model using different SFH in the simulations, this means that we will place the star clusters at different times into the simulation and see the differences between each SFH, and finally we will analyze the kinematic and morphology of the final objects to compare with observational data and with the previous work.

1.9 SUPERBOX

SUPERBOX (Fellhauer et al. 2000) is a particle-mesh code with moving high-resolution subgrids, which stay focus on the object of interest. A particle-mesh code neglects by default close encounters between the particles (which are rather representations of the phase-space than actual stars) and is therefore called collision-less. With a collision-less code it is possible to simulate galaxies without having to use the actual number of stars (10^{10} approx). SUPERBOX provides two levels of high resolu-

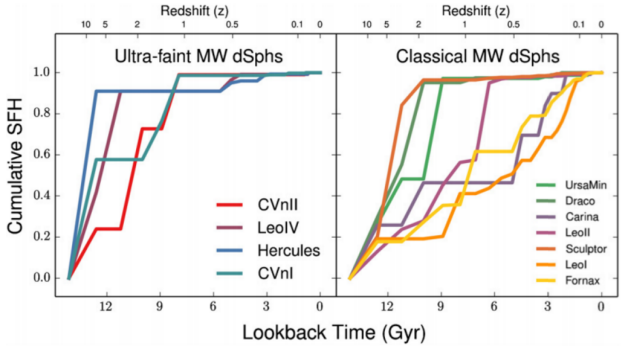

Figure 1.10: Star formation histories of some dwarf spheroidal galaxies obtained analyzing the stars of the main sequence with the Hubble Space Telescope (Weisz et.al 2014). In this plots we can see that the SFH of dSph galaxies are diverse, ranging between SFH constant until today like Fornax or Leo I to intense star-burst, where all the stars of the galaxy were formed almost at the same time as we can see in the Sculptor galaxy or in the ultra faint MW dSph, the work did by Assmann et al. could be approximated to a SFH with a high star-burst.

tion sub-grids, providing high spatial resolution at the places of interest without wasting computational resources. Another feature of this code is its speed and its resourcefulness, i.e. the small amount of memory it needs. This code enables its user to simulate objects with millions of particles, to ensure high resolution, on normal desktop computers.

Chapter 2

SUPERBOX

To compute the gravitational potential the code resolves the density and uses a stationary Green's function to solve the Poisson equation 2.1 in Fourier space via a Fast Fourier Transformation (FTT).

$$\nabla^2\phi = 4\pi G\rho \tag{2.1}$$

where $\rho(\vec{r})$ is the density at a distance r from the center of coordinates, and G is the gravitational constant. This potential at the same time is related to the force $F(\vec{r})$ exerted over a particle located at a distance r from the center through the following expression:

$$\vec{F}(\vec{r}) = -\vec{\nabla}\Phi(\vec{r}) \tag{2.2}$$

The way of solving equation 2.1 is the core of the Particle-Mesh method. To do this, the method takes the whole simulation region and divides it into a Cartesian 3-D grid of N components (or grid-cells) per dimension. Therefore, the values of the density function $\rho(\vec{r})$ will depend now on the grid-cell where we are, and will be denoted by ρ_{ijk}, with i,j,k being the i-th grid-cell in the x axis, j for the y axis, and k for the z axis. Same procedure goes for the potential $\Phi(\vec{r})$.

Poisson's equation is then solved for the density array:

$$\Phi_{ijk} = G\sum_{a,b,c=0}^{N-1} \rho_{abc}\cdot H_{a-i,b-j,c-k}, \qquad i,j,k = 0,...,N-1 \tag{2.3}$$

Where H_{ijk} is a Green's Function. Considering unit-sized grid-cell, the Green's function can take the form:

$$H_{ijk} = \frac{1}{\sqrt{i^2 + j^2 + k^2}}, \qquad i, j, k = 0, ..., N \tag{2.4}$$

where a value of

$$H_{0,0,0} = \frac{3}{4} \tag{2.5}$$

is adopted in SUPERBOX because a better numerical performance in energy conservation (Fellhauer et al. 2000)

In order to minimize the number of calculations involved in this procedure, a Fast Fourier Transform (FFT) is applied for both density array and the Green's function. The new potential and Green's function grids therefore will change to:

$$\hat{\rho}_{abc} = \sum_{i,j,k=0}^{N-1} \rho_{ijk} \cdot exp\left(-\sqrt{-1}\frac{2\pi}{N}(ai + bj + ck)\right) \tag{2.6}$$

and

$$\hat{H}_{abc} = \sum_{i,j,k=0}^{N-1} H_{ijk} \cdot exp\left(-\sqrt{-1}\frac{2\pi}{N}(ai + bj + ck)\right) \tag{2.7}$$

respectively. To perform the FFT, SUPERBOX uses the procedure and code from Press et al. (1985), which makes the code portable. The performance of the code can be increased further through another FFT routine (Fellhauer, 2000). It is important to note that the FFT is applied just once for the Green's Function, in contrast to the density grid where the FFT must be calculated for each time-step.

The grid-based potential therefore can be calculated as:

$$\Phi_{ijk} = \frac{G}{N^3} \sum_{a,b,c=0}^{N-1} \hat{\rho}_{abc} \cdot \hat{H}_{abc} \cdot exp\left(\sqrt{-1}\frac{2\pi}{N}(ai + bj + ck)\right) \tag{2.8}$$

and the accelerations therefore can be computed as in equation 2.2 though numerical differentiation. The new positions are then calculated using a Leap-Frog scheme, a scheme of the procedure is shown in Figure 2.1

2.1 The grids

For each galaxy, 5 grids with 3 different resolutions are used. This is possible by invoking the additivity of the potentials (Fig 2.2). The five grids are as follows:

- Grid 1 is the high-resolution grid which resolves the center of the galaxy. it has a length of $2 \times R_{core}$ in one dimension. In evaluating the densities, all particles of the galaxy within $r \leq R_{core}$ are stored in this grid.
- Grid 2 has an intermediate resolution to resolve the galaxy as a whole. The length is $2 \times R_{out}$, but only particles with $r \leq R_{core}$ are stored here, i.e. the same particles as are also stored in grid 1.
- Grid 3 has the same size and resolution as grid 2, but it only contains particles between $Rcore < r \leq R_{out}$.
- Grid 4 has the size of the whole simulation area (i.e 'local universe' whit $2 \times R_{system}$), and has the lowest resolution. It is fixed. Only particles of the galaxy with $r \leq R_{out}$ are stored in grid 4.
- Grid 5 has the same size and resolution as grid 4. This grid treats the escaping particles of a galaxy, and contains all particles with $r > R_{out}$.

Grids 1 to 3 are focused on a common center of the galaxy and move with it through the 'local universe'.
The inner and middle grid can be positioned and tracked considering two schemes. One scheme centers the grids on the density maximum of each galaxy at each step. The position of the density maximum is found by constructing a sphere of neighbours centered on the densest region, in which the center of mass is computed. This is performed iteratively. The other scheme is to center the grids during run-time on the position of the center of the mass of each galaxy using all its particles remaining in the computation.

Each of the grids has its associated potential $\Phi_1, \Phi_2, ..., \Phi_5$, and invoking the additivity of the potential, we can calculate the parameter

as follows:

$$\Phi(r) =$$
$$[\theta(R_{core}-r)\cdot\Phi_1+\theta(r-R_{core})\cdot\Phi_2+\Phi_3]\cdot(R_{out}-r)+\theta(r-R_{out})\cdot\Phi_4+\Phi_5$$
$$\Phi(R_{core}) = \Phi_1 + \Phi_3 + \Phi_5$$
$$\Phi(R_{out}) = \Phi_2 + \Phi_3 + \Phi_5$$

where $\theta(\xi) = 1$ when $\xi > 0$ and $\theta(\xi) = 0$ otherwise. Then, to calculate the accelerations of the particles in the simulations, we have that:

- If the particle is inside R_{core}, then the potentials calculated in grids 1, 3 and 5 are used.
- If the particle is between R_{core} and R_{out}, then the potentials calculated in grids 2, 3 and 5 are used.

Finally, any particle that escapes the simulation region is discarded for the rest of the calculations.

When simulating many objects at the same time, and as long as they are apart from each other, they will feel the potential only from their outer grids. But when approaching, their inner grids will overlap, generating high-resolution calculations and thus getting a better description of their interaction.

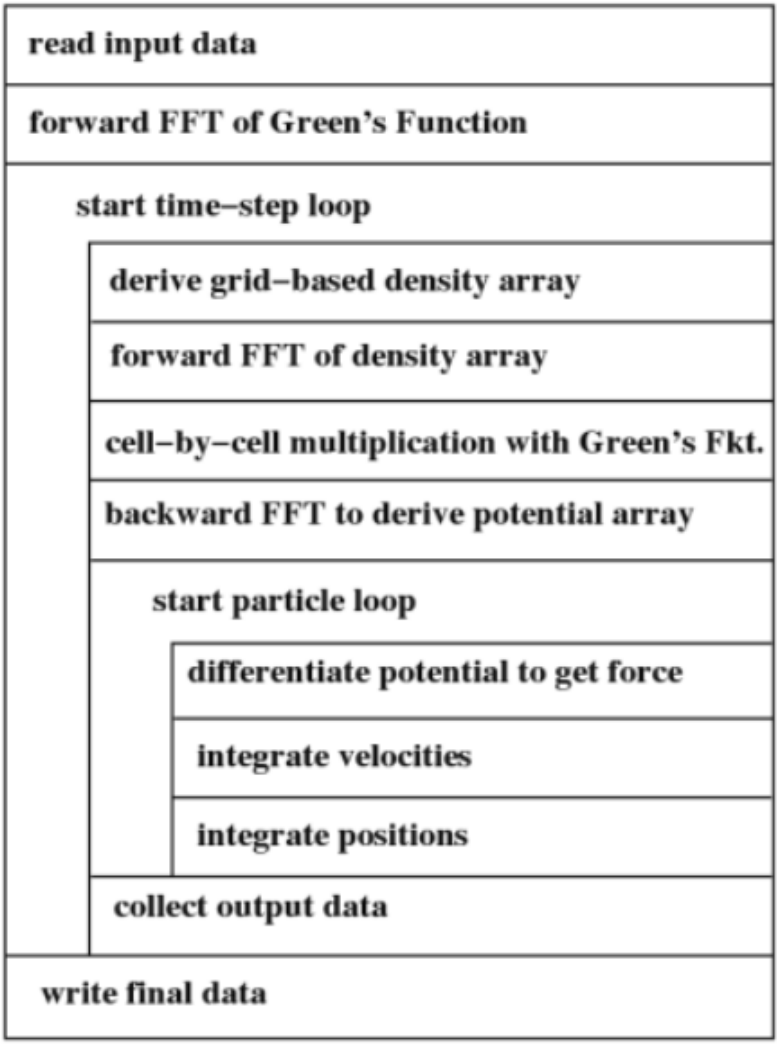

Figure 2.1: Float-chart for SUPERBOX

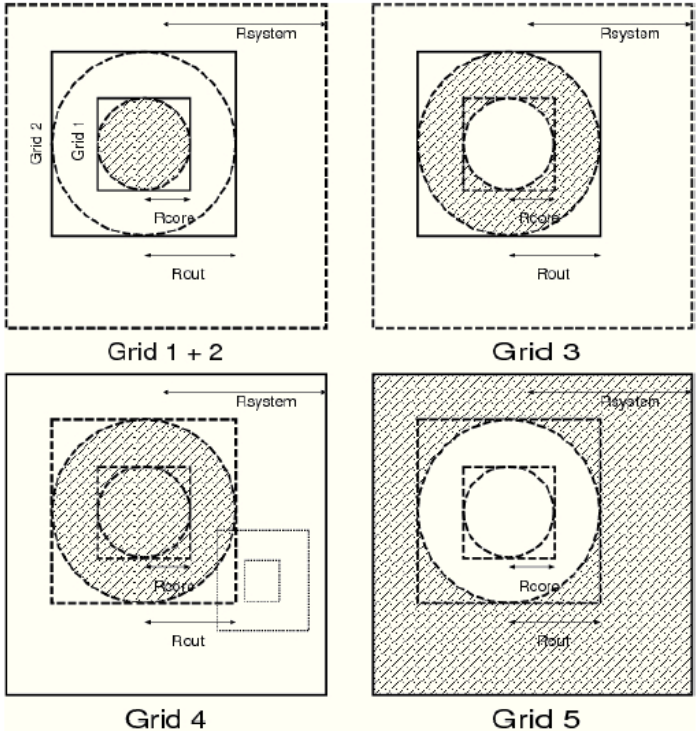

Figure 2.2: The five grids of SUPERBOX. In each panel, solid lines highlight the particular grid. Particles are counted in the shaded areas of the grids. The lengths of the arrows are $(N/2) - 2$ grid-cells. In the bottom left panel, the grids of a hypothetical second galaxy are also shown as dotted lines.

Chapter 3

Setup

We consider the same setup as the fiducial model from Assmann et al. (2013), with the difference that we will place the star cluster at different moments in the simulation to mimic a star formation history.

i Simulations with a cusped dark matter halo, as cosmological simulations predict, use a Navarro, Frenk & White (NFW; Navarro 1997) profile, using 1,000,000 particles according to the recipe described in Dehnen & McLaughlin (2005). We use a scale-length for the halo of $R_{\rm s,h} = 1$ kpc and define an enclosed halo mass within 500 pc of $M_{500} = 10^7$ $M_\odot$, following the fiducial model described in Assmann et al. (2013a). Using a standard value for $H_0 = 70 {\rm km\,s^{-1} Mpc^{-1}}$ and $r_{\rm vir} = r_{200}$, we obtain a virial radius of $r_{\rm vir} = 12.7$ kpc, i.e. the concentration of the halo is $c = 12.7$, which agrees with the range of values found with dSph galaxies of 5-20. The total mass of the halo out to the virial radius amounts to 2.3×10^8 $M_\odot$.

ii For the simulations with a cored dark matter halo, as observations predicts, we use a Plummer sphere profile, using 1,000,000 of particles, again we use a scale-length (Plummer radius) of $R_{\rm s,h} = 1$ kpc, and an enclosed mass within 500 pc of $M_{500} = 10^7$ $M_\odot$. For the Plummer profile we use a cutt-off radius of $R_{\rm cut} = 5$ kpc, which contains more than 94% of the total mass of a Plummer sphere, accounting in our case to a total mass of the halo of 1.1×10^8 $M_\odot$.

iii For the luminous component, the star clusters, we use $N = 30$ star clusters. This number is chosen arbitrarily, because the previous results of Assmann et al. (2013a,b), show no significant differences using different numbers of SCs. As it is claimed that dSph galaxies had low star formation rates and therefore also a low SFE (Bressert et al. 2010), we form rather low mass open clusters and associations than massive SCs. Each SC is modeled as a Plummer sphere (Plummer 1911), using 100,000 particles using the recipe of Aarseth, Henon & Wielen (1974). The SCs have a Plummer radius (half light radius) of $R_{\rm pl} = 4$pc and a cut-off radius of 25pc. This is similar to the radii found for young SCs in the Antennae (Withmore et al. 1999). We perform simulations where all SCs have a SFE=30% and simulations with SFE=20%, therefore the initial mass of each SC in its embedded phase is $5 \times 10^4 {\rm M}_\odot$ with a SFE=30% and $7.5 \times 10^4 {\rm M}_\odot$ with a SFE=20%. We mimic the gas-expulsion of the SCs by artificially reducing the mass of each particle until the final mass is reached after one crossing time, i.e. 4 Myr. As the mass in lost gas is negligible compared to the DM mass we do not take this mass further into account. The final mass in stars after this mass loss amounts to $4.5 \times 10^5 {\rm M}_\odot$, which is a typical stellar mass of one of the classical dSph (e.g. Mateo M. (1998)). Note that this results in a particle resolution in our simulation which is slightly better than reality, i.e. more star particles than actual stars (see explanation below).

iv The star clusters themselves are distributed in virial equilibrium inside the halo according to their Plummer distribution. This is made for simplicity, because we do not know exactly in which virial state the SCs form with respect to the halo and we expect more star cluster to form in the center than in the outer parts. The distribution has a scale-length of $R_{\rm pl,sc} = 0.25$ kpc and a cut-off radius of $R_{\rm cut-off} = 1.125$ kpc. The initial orbital velocities are obtained from the Jeans equation:

$$\sigma^2_{r,i}(r) = \frac{1}{\rho_i(r)} \int_r^{rc} \frac{GM_{tot}(r')}{r^2} \rho_i(r') dr', \qquad (3.1)$$

where $M_{\rm tot}$ correspond to the total mass given by the sum of the

mass of all SCs and the mass of the DM halo. Also we do not take into account that the SCs might form in a disc-like structure showing angular momentum in their distribution, as we assume that the gas distribution on those small scales of a dSph is rather supported by pressure than rotation. With this assumption we differ from most of the previous models in which dSph galaxies are simply the evolutionary outcome of harassed dwarf disc galaxies, which lost their angular momentum because of gravitational forces. Our model gives a natural explanation to why we see dSph galaxies in the Local Group far away from any major galaxies.

v To mimic the star formation histories we insert the star clusters at different times into the simulations. We probe four different star formation histories. Figure 3.1 shows the SFHs used in this project. The first is a constant SFH in which we insert the star clusters one by one over the whole 10 Gyr of evolution in equally spaced time-intervals. The second SFH mimics a linearly declining SFR and the third a quadratic decline in SFR. I.e. in both cases the majority of SCs are inserted at early times of the simulation and only a few get inserted at late times. The last SFH mimics a double burst as implied for Tucana. Half of the SCs get inserted at the beginning of the simulation and the second half after 5 Gyr, i.e. half of the simulation time. For the common SFH of dSph galaxies, the single burst at very early times, we refer to the models of Assmann et al. (2013a,b) in which the simulations start with all SCs from the beginning.

We simulate the cluster complex within the DM halo using the particle mesh code SUPERBOX (Fellhauer et al. 2000) , SUPERBOX has two levels of high resolution sub-grids. The highest resolution grid has a resolution (i.e. cell-length) of 8.3 pc for the dark matter halos and 0.41 pc for the star clusters and covers the central area of the halo or the SCs completely, respectively. The medium resolution grid has a cell-length of 41 pc for the DM halo and 4.1 pc for the SCs. Finally the outermost grid covers the complete area beyond the virial radius of the dark matter halo with a resolution of 830 pc. The time-step is fixed at 0.25 Myr to resolve the internal

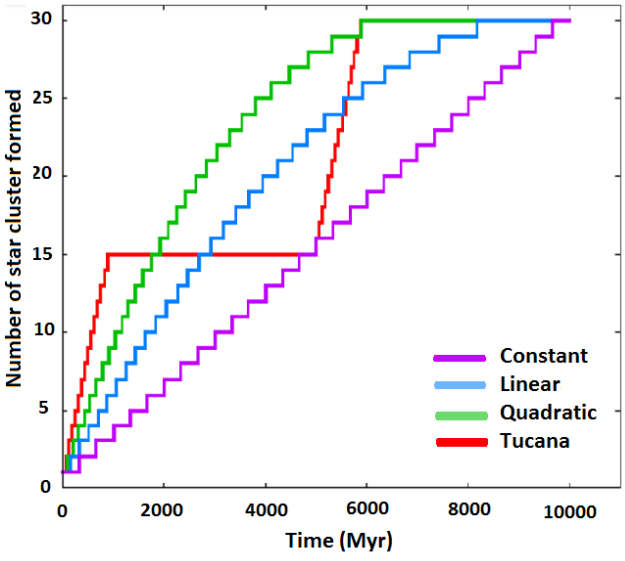

Figure 3.1: Star formation histories used in this project.

dynamics of the SCs and we simulate for 10 Gyr. As the SCs dissolve immediately and therefore the two-body relaxation effects are not important. we are able to use a fast particle-mesh code (Which here are rather representations of the phase space than actual single stars) and is therefore called collisionless. A particle mesh-code naturally neglects close encounters between particles. That the particles are phase-space representations make it (in our case) possible to actually use more particles than actual stars. With the same reasoning we can model the DM halo without using an actual number of possible DM particles.

In Figure 3.2 we show the snapshots of one of our simulations to show the process of evolution and dissolution of the SCs to form a final object with characteristics of a classical dSph after 10 Gyr.

In the next section we will summarize the results of all our simulations.

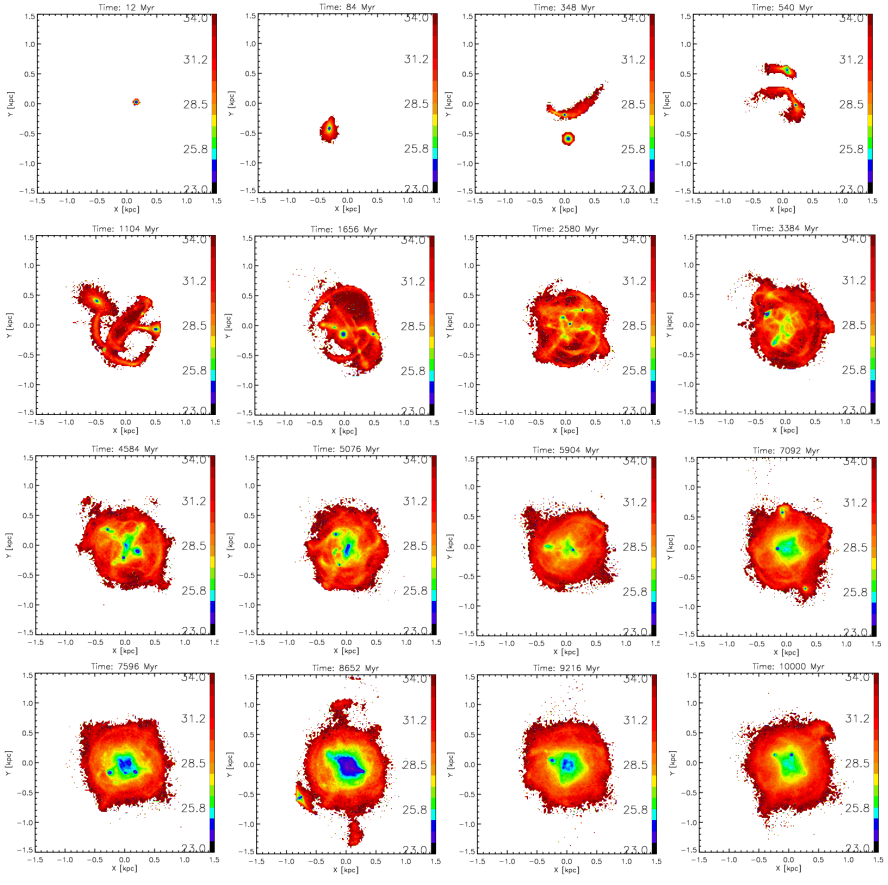

Figure 3.2: Snapshots of a simulation of this project, We simulate for 10 Gyr, but we will put the star clusters in different moments of the simulations. In the figure we can see how the star cluster dissolve and mix in the center of the dark matter halo. This simulations has a constant SFH, cusped DM profile and the SFE is 30%.

Chapter 4

Results

We perform 64 simulations in total, 4 for each SFH, constant (cte), linear(lin), quadratic (quad) and Tucana (tuc) ie., two burst, each of them with a SFE of 20% and 30 %, and all of these simulations with a DM profile following a NFW or with a Plummer sphere profile. We use 4 different sets of initial positions and velocities for the star clusters in each DM profile. The goal is to study the differences between the SFH, and show that our scenario for the formation of dSph galaxies leads to objects that resemble the properties of these galaxies, even when we use quite different initial conditions and different SFH, thus showing that the scenario we propose is plausible. In Table 4.1 and 4.2 we give the name and parameters of each simulation. In Figure 4.1, we show a set of some characteristics of the final objects of four different simulations taken as examples, to show that they can resemble the properties of classical dSph, in the next subsections we will focus on the analysis of the surface brightness profile, the velocity dispersion, the shape of the final object and the surviving SCs.

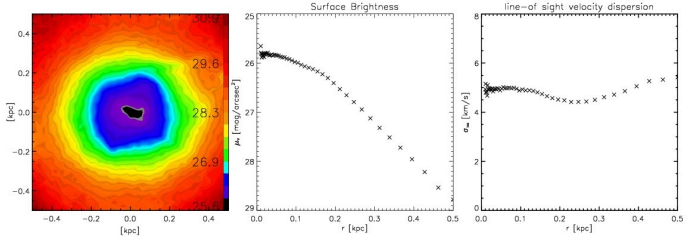

(a) Linear SFH, SFE=20% and cusped DM halo

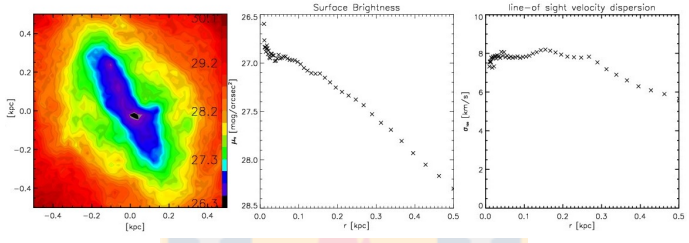

(b) Quadratic SFH, SFE=20% and cusped DM halo

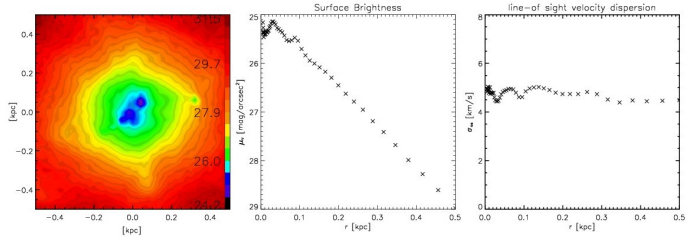

(c) Constant SFH, SFE=30% and cusped DM halo

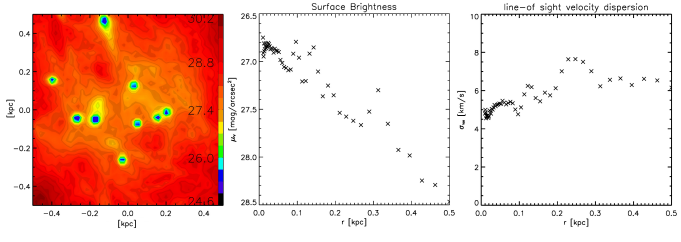

(d) Constant SFH, SFE=30% and cusped DM halo

Figure 4.1: Characteristics of the final object inside a radius of 500 pc, the left panel is the shape of the final object with a color bar for the magnitude, the center panel is the surface brightness and the right panel is the velocity dispersion, under each set of images we see the initial conditions of the simulation.

Table 4.1: Simulations with a Navarro Frank & White profile for the Dark matter halo, here we show the initial conditions used in our models.

N°	Simulation	NFW/Pl	SFH	SFE[%]	I.C
01	1NFWcte20	NFW	cte	20	1
02	1NFWlin20	NFW	lin	20	1
03	1NFWquad20	NFW	quad	20	1
04	1NFWtuc20	NFW	tuc	20	1
05	2NFWcte20	NFW	cte	20	2
06	2NFWlin20	NFW	lin	20	2
07	2NFWquad20	NFW	quad	20	2
08	2NFWtuc20	NFW	tuc	20	2
09	3NFWcte20	NFW	cte	20	3
10	3NFWlin20	NFW	lin	20	3
11	3NFWquad20	NFW	quad	20	3
12	3NFWtuc20	NFW	tuc	20	3
13	4NFWcte20	NFW	cte	20	4
14	4NFWlin20	NFW	lin	20	4
15	4NFWquad20	NFW	quad	20	4
16	4NFWtuc20	NFW	tuc	20	4
17	1NFWcte30	NFW	cte	30	1
18	1NFWlin30	NFW	lin	30	1
19	1NFWquad30	NFW	quad	30	1
20	1NFWtuc30	NFW	tuc	30	1
21	2NFWcte30	NFW	cte	30	2
22	2NFWlin30	NFW	lin	30	2
23	2NFWquad30	NFW	quad	30	2
24	2NFWtuc30	NFW	tuc	30	2
25	3NFWcte30	NFW	cte	30	3
26	3NFWlin30	NFW	lin	30	3
27	3NFWquad30	NFW	quad	30	3
28	3NFWtuc30	NFW	tuc	30	3
29	4NFWcte30	NFW	cte	30	4
30	4NFWlin30	NFW	lin	30	4
31	4NFWquad30	NFW	quad	30	4
32	4NFWtuc30	NFW	tuc	30	4

Table 4.2: Simulations with a Plummer sphere profile for the dark matter halo, here we show the initial conditions used in our models.

N°	Simulation	NFW/Pl	SFH	SFE[%]	I.C
33	1Plcte20	Pl	cte	20	1
34	1Pllin20	Pl	lin	20	1
35	1Plquad20	Pl	quad	20	1
36	1Pltuc20	Pl	tuc	20	1
37	2Plcte20	Pl	cte	20	2
38	2Pllin20	Pl	lin	20	2
39	2Plquad20	Pl	quad	20	2
40	2Pltuc20	Pl	tuc	20	2
41	3Plcte20	Pl	cte	20	3
42	3Pllin20	Pl	lin	20	3
43	3Plquad20	Pl	quad	20	3
44	3Pltuc20	Pl	tuc	20	3
45	4Plcte20	Pl	cte	20	4
46	4Pllin20	Pl	lin	20	4
47	4Plquad20	Pl	quad	20	4
48	4Pltuc20	Pl	tuc	20	4
49	1Plcte30	Pl	cte	30	1
50	1Pllin30	Pl	lin	30	1
51	1Plquad30	Pl	quad	30	1
52	1Pltuc30	Pl	tuc	30	1
53	2Plcte30	Pl	cte	30	2
54	2Pllin30	Pl	lin	30	2
55	2Plquad30	Pl	quad	30	2
56	2Pltuc30	Pl	tuc	30	2
57	3Plcte30	Pl	cte	30	3
58	3Pllin30	Pl	lin	30	3
59	3Plquad30	Pl	quad	30	3
60	3Pltuc30	Pl	tuc	30	3
61	4Plcte30	Pl	cte	30	4
62	4Pllin30	Pl	lin	30	4
63	4Plquad30	Pl	quad	30	4
64	4Pltuc30	Pl	tuc	30	4

4.1 Surface density profile

To fit the observed surface brightness curves of the dSph galaxies we consider the followings profiles, King (without tidal radius), Plummer and Sérsic profiles according to the following formulas:

- King:

$$\Sigma(R) = \frac{\Sigma_0}{1 + (\frac{R}{R_c})^2} \tag{4.1}$$

  Where the free parameters Σ_0 and R_c are the central surface density and the core radius, respectively. This profile is widely used by observers to fit the surface brightness, we consider only equation 5.2 from King (1962) for the inner parts and avoid fitting tidal radii.

- Plummer:

$$\Sigma(R) = \frac{\Sigma_{eff}}{(1 + \frac{R}{R_{pl}}^2)^2} \tag{4.2}$$

  Where R_{pl} is the Plummer radius, which corresponds to the half-light radius and Σ_{eff} is the surface density within of the half-light radius. As some initial conditions depends on a Plummer sphere distribution is a good idea to try to fit with this profile the results.

- Sérsic:

$$\Sigma(R) = \Sigma_{eff} exp\left(-b_n\left[\left(\frac{R}{R_{eff}}\right)^{1/n} - 1\right]\right) \tag{4.3}$$

$$b_n = 1.9992n - 0.3271,$$

  Where R_{eff} is the effective radius and Σ_{eff} is the surface density at the effective radius. The index n gives information about the shape of the dSph galaxy. In the case $n \approx 1$, we will have an exponential shaped profile for the surface density distribution. This profile has the advantage of having a 3 parameter, so it is easier

to adjust this profile to the data, a value of $n \approx 1$ is used in the observations to fit the surface brightness profile of dSph.

Surface brightness profiles show integrated light along a line of sight. As we do not know along which line of sight our object may be observed, we can calculate a mean value out of three possible line of sight along Cartesian coordinates axis x, y and z. The results obtained for simulations with a NFW DM profile and Plummer profile are shown in Table 4.3 and Table 4.4 respectively.

For the simulation with a NFW DM profile is clear to see that the surface brightness profile is highly dependent on the initial conditions of the SCs, this is because the SCs dissolve very quickly and then stay orbiting the center of the DM halo, even using recent star formation we have enough time to dissolve the latest SCs, and even using a SFE of 20% or 30% the results are almost the same because most of the SCs are dissolved and the stars are distributed in all the galaxy.

In simulations with a Plummer profile we do not see that trend because the SCs need more time to get dissolved, this is a consequence of that Plummer models have central crossing-times larger than models with NFW profiles and less interactions/time to erase substructures, and undissolved SCs create bumps and wiggles in the Surface brightness profile that spread the values obtained when we fit the results.

In all simulations the best fit is the Sersic profile, this profile is easier to fit because it has 3 free-parameters, the values of $n \approx 1$ means that our resulting objects have approximately an exponential surface brightness distribution, like the dSph galaxies of the Local Group (Caon et al. 1993; Jerjen, Binggeli & Freeman 2000; Walcher et al. 2003).

In Figure 4.2, we show the correlation between the King, Plummer and the three parameters of the Sèrsic profile (Σ_{eff}, n and R_{eff}) fitted to our models with the parameters of SFH for both DM halo distribution and also we calculate the mean value between all the SFH. In the left panels we see the mean values for surface bright parameters (Σ_0 for King and Σ_{eff} for Plummer and Sersic), the right panels are for the radii parameters (R_c, R_{pl} and R_{eff}), the bottom panel is the n index for the Sersic fit, we use red lines for cusped DM haloes and black for cored models.

By analyzing the data we do not find any dependency between the fitting parameters on the SFH or the SFE used and in our models the Sérsic profile was the best fit to our data.

Figure 4.2 shows clearly that cusped DM halo give us higher values for the brightness parameters Σ, and lower for the radii R than our cored DM models, this is because a cusped profile has a higher density in the center and the stars are more likely to orbit in the nearest part of the DM halo than in a cored DM profile.

We see that the Sersic index n has no dependency on any initial parameter. It shows always mean values around 1, independently of the SFH, SFE or DM halo. This means that our resulting objects have approximately an exponential surface brightness distribution, like the dSph galaxies of the Local Group (Walcher C. J et.al 2003, Jerjen H. et.al 2000, Caon N. et.al 1993).

Using the Sersic profile the mean values obtained, taking into account all the simulations with a NFW DM halo is n=0.73±0.159, $R_{eff} = 245 \pm 26$pc and $\Sigma_{eff} = 0.766 \pm 0.111$ $M_\odot/pc^2$, and for cored models the mean values are n=0.843±0.289, $R_{eff} = 523 \pm 195$pc and $\Sigma_{eff} = 0.196 \pm 0.068 M_\odot/pc^2$.

Photometrical observations of the dSph galaxies in the Local Group (Irwin M. et.al 1995 and Mateo M. et.al 1998) show that we can find different sizes of these galaxies. For example, the effective radius of Draco, Umi, Sculptor and Fornax are 180, 200, 110 and 460 pc, respectively (Mateo M. 1998, Irwin M. et al. 1995).

Table 4.4: Fit of the surface brightness profile considered for each simulation with a Plummer DM profile. We show the values obtained by fitting a King, Plummer and Sersic profile.

N°	Simulation	King		Plummer		Sersic		
		Σ_0 $[\frac{M_\odot}{pc^2}]$	R_c [kpc]	Σ_0 $[\frac{M_\odot}{pc^2}]$	R_{pl} [kpc]	Σ_{eff} $[\frac{M_\odot}{pc^2}]$	R_{eff} [kpc]	n
33	1Plcte20	0.703	0.293	0.656	0.513	0.205	0.469	0.825
34	1Pllin20	0.766	0.271	0.711	0.477	0.202	0.462	0.903
35	1Plquad20	0.783	0.269	0.726	0.473	0.212	0.451	0.883
36	1Pltuc20	0.778	0.279	0.729	0.483	0.257	0.408	0.734
37	2Plcte20	0.749	0.279	0.695	0.493	0.189	0.493	0.933
38	2Pllin20	0.798	0.266	0.738	0.468	0.200	0.471	0.939
39	2Plquad20	0.701	0.295	0.657	0.513	0.206	0.468	0.818
40	2Pltuc20	0.710	0.300	0.669	0.517	0.234	0.440	0.736
41	3Plcte20	0.478	0.354	0.452	0.609	0.130	0.593	0.870
42	3Pllin20	0.457	0.370	0.433	0.635	0.127	0.609	0.855
43	3Plquad20	0.476	0.357	0.451	0.614	0.130	0.596	0.869
44	3Pltuc20	0.488	0.354	0.464	0.605	0.149	0.546	0.789
45	4Plcte20	0.627	0.304	0.587	0.528	0.159	0.533	0.929
46	4Pllin20	0.546	0.343	0.516	0.591	0.159	0.547	0.824
47	4Plquad20	0.560	0.339	0.530	0.581	0.172	0.520	0.786
48	4Pltuc20	0.593	0.314	0.557	0.546	0.151	0.552	0.924
49	1Plcte30	0.683	0.326	0.674	0.526	0.336	0.350	0.504
50	1Pllin30	0.724	0.301	0.712	0.493	0.299	0.374	0.600
51	1Plquad30	0.745	0.298	0.732	0.490	0.288	0.387	0.641
52	1Pltuc30	0.722	0.312	0.713	0.505	0.341	0.346	0.526
53	2Plcte30	0.642	0.336	0.631	0.551	0.241	0.446	0.657
54	2Pllin30	0.830	0.241	0.800	0.417	0.046	1.427	1.894
55	2Plquad30	0.836	0.244	0.811	0.414	0.166	0.539	1.045
56	2Pltuc30	0.813	0.253	0.793	0.421	0.221	0.440	0.847
57	3Plcte30	0.464	0.394	0.458	0.634	0.206	0.456	0.562
58	3Pllin30	0.577	0.299	0.564	0.497	0.149	0.538	0.874
59	3Plquad30	0.478	0.368	0.470	0.604	0.160	0.534	0.720
60	3Pltuc30	0.507	0.348	0.498	0.572	0.183	0.483	0.677
61	4Plcte30	0.614	0.344	0.608	0.550	0.309	0.359	0.494
62	4Pllin30	0.664	0.299	0.651	0.493	0.193	0.483	0.807
63	4Plquad30	0.608	0.321	0.596	0.528	0.185	0.501	0.780
64	4Pltuc30	0.909	0.176	0.868	0.307	0.064	0.927	1.728

Table 4.3: Fit of the surface brightness profile considered for each simulation with a NFW DM profile. We show the values obtained by fitting a King, Plummer and Sersic profile.

Nº	Simulation	King Σ_0 $[\frac{M_\odot}{pc^2}]$	R_c [kpc]	Plummer Σ_0 $[\frac{M_\odot}{pc^2}]$	R_{pl} [kpc]	Sersic Σ_{eff} $[\frac{M_\odot}{pc^2}]$	R_{eff} [kpc]	n
01	1NFWcte20	2.298	0.167	2.232	0.279	0.808	0.234	0.69
02	1NFWlin20	1.978	0.195	1.936	0.321	0.891	0.227	0.54
03	1NFWquad20	1.9982	0.188	1.947	0.312	0.765	0.246	0.64
04	1NFWtuc20	2.0377	0.184	1.986	0.306	0.778	0.242	0.64
05	2NFWcte20	2.502	0.151	2.417	0.255	0.767	0.234	0.78
06	2NFWlin20	2.456	0.154	2.378	0.259	0.796	0.229	0.74
07	2NFWquad20	2.3834	0.160	2.312	0.268	0.829	0.226	0.70
08	2NFWtuc20	2.446	0.158	2.373	0.264	0.869	0.219	0.69
09	3NFWcte20	1.541	0.216	1.504	0.360	0.574	0.292	0.66
10	3NFWlin20	1.374	0.246	1.348	0.404	0.615	0.288	0.55
11	3NFWquad20	1.426	0.239	1.400	0.393	0.640	0.280	0.55
12	3NFWtuc20	1.466	0.234	1.438	0.384	0.650	0.275	0.55
13	4NFWcte20	3.238	0.124	3.089	0.213	0.699	0.249	1.02
14	4NFWlin20	3.0516	0.135	2.933	0.230	0.848	0.226	0.85
15	4NFWquad20	2.811	0.145	2.711	0.246	0.842	0.229	0.79
16	4NFWtuc20	2.739	0.150	2.650	0.253	0.921	0.218	0.72
17	1NFWcte30	2.462	0.162	2.393	0.271	0.904	0.220	0.67
18	1NFWlin30	2.262	0.172	2.199	0.287	0.828	0.233	0.67
19	1NFWquad30	2.3099	0.163	2.003	0.305	0.712	0.254	0.74
20	1NFWtuc30	2.257	0.168	2.189	0.282	0.730	0.250	0.74
21	2NFWcte30	2.969	0.130	2.846	0.222	0.723	0.238	0.93
22	2NFWlin30	2.7319	0.141	2.266	0.274	0.746	0.238	0.83
23	2NFWquad30	2.628	0.149	2.544	0.250	0.878	0.217	0.72
24	2NFWtuc30	2.446	0.158	2.373	0.264	0.869	0.219	0.69
25	3NFWcte30	1.571	0.222	1.542	0.364	0.716	0.257	0.54
26	3NFWlin30	1.555	0.226	1.525	0.372	0.678	0.269	0.56
27	3NFWquad30	1.588	0.218	1.553	0.361	0.630	0.279	0.62
28	3NFWtuc30	1.670	0.208	1.630	0.346	0.605	0.285	0.67
29	4NFWcte30	3.523	0.120	3.367	0.205	0.845	0.222	0.95
30	4NFWlin30	3.4832	0.116	3.293	0.203	0.512	0.306	1.30
31	4NFWquad30	3.150	0.134	3.028	0.228	0.898	0.219	0.83
32	4NFWtuc30	3.066	0.138	2.954	0.233	0.932	0.215	0.79

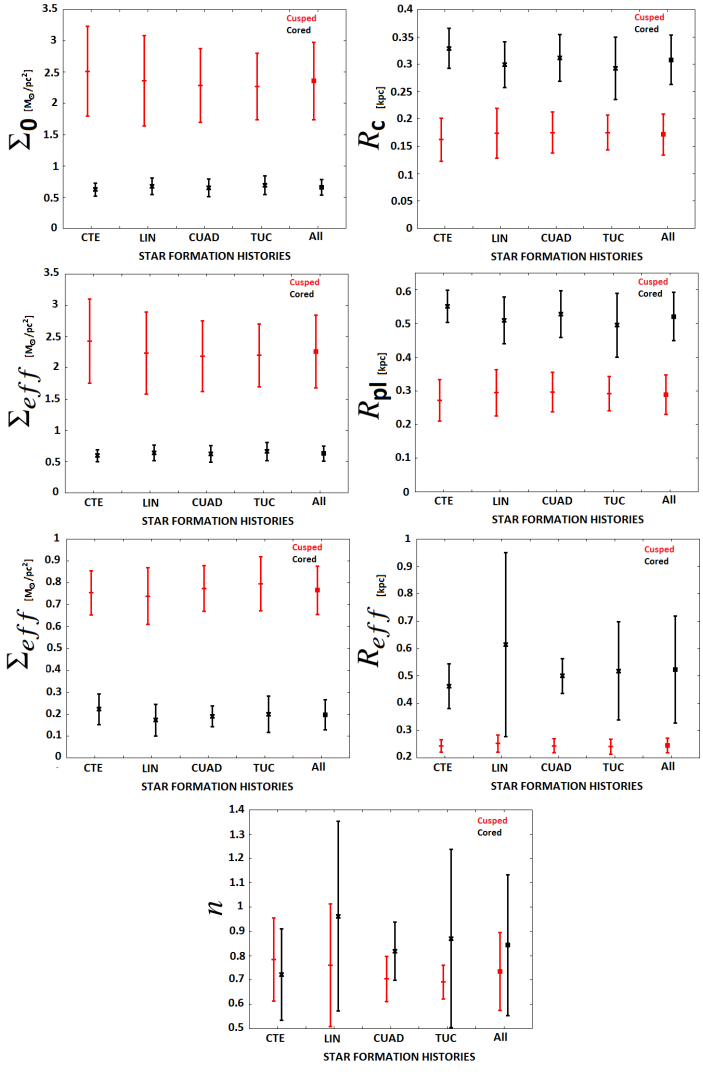

Figure 4.2: Fit of the surface brightness profile: The left panels are for brightness parameters and right panels for Radii parameters for the fit, the bottom panel is for the n index of the Sersic profile, red color is for cusped and black is for cored DM profile. In the X-axis we plot the SFH and the mean values of all of them, to show that we did not find any dependence on the SFH used.

4.2 Shape of the final object

It is possible to characterize the shape of our resulting objects considering the parameters introduced by Conselice et al. (2003), they are the clumpiness and the asymmetry, and also we measure the weight of the clumps, the ellipticity, and the isophotal parameter A_4, we show the values for these parameters for each simulation in Table 4.5 and 4.6 for a cusped DM halo and a cored DM halo respectively.

4.2.1 Clumpiness C

The parameter C is a measure which indicates the inhomogeneity of the distribution of the luminous component of the galaxy. We measure this parameter, for the final objects formed in our simulations, according to the work of Conselice et al. (2003), as is shown in Equation 4.4.

$$C = \frac{\Sigma_{allpix} m_{residual,pixel}}{\Sigma_{allpix} m_{original,pixel}} \tag{4.4}$$

The clumpiness is defined as the sum of all positive fluxes from the residuals divided by the sum of fluxes of the original data, to get the residuals image we subtract a model fit obtained using the routine ELLIPSE from IRAF (see Figure 4.3).

In Figure 4.4, we show the relationship between the clumpiness of the model and the SFH, SFE and DM distribution. Left panel is from cusped DM halo models and the right panel is for cored DM halo, black crosses are for SFE=30% and red crosses for SFE=20% and in the x-axis we plot the SFH. The presence of surviving SCs give us fitted images which are not good enough because the ELLIPSE routine can not find the center of the ellipse easily, that give us larger error bars in our plots in models with many surviving SCs.

Table 4.5: Shape parameters for simulations following a NFW distribution for the DM halo. The third column is the clumpiness value, fourth is weight of the clumps, fifth is asymmetry, sixth is the ellipticity, seven is the isophotal parameter A_4 and the last column is the number of surviving SCs.

Nº	Simulation	C	Σ_C $[\frac{M_\odot}{pc^2}]$	Asymmetry	e	A_4	Surv SC(s)
01	1NFWcte20	0.046	1.282	0.219	0.232	-0.013	0
02	1NFWlin20	0.028	0.274	0.225	0.173	-0.024	0
03	1NFWquad20	0.019	0.180	0.262	0.173	-0.0080	0
04	1NFWtuc20	0.019	0.158	0.223	0.058	-0.043	0
05	2NFWcte20	0.046	3.328	0.317	0.091	0.019	0
06	2NFWlin20	0.019	0.202	0.256	0.115	-0.011	0
07	2NFWquad20	0.014	0.110	0.227	0.034	0.0054	0
08	2NFWtuc20	0.018	0.125	0.336	0.118	-0.0039	0
09	3NFWcte20	0.048	0.600	0.166	0.197	-0.031	0
10	3NFWlin20	0.036	0.269	0.246	0.074	-0.073	0
11	3NFWquad20	0.025	0.125	0.167	0.043	0.083	0
12	3NFWtuc20	0.037	0.198	0.218	0.098	-0.038	0
13	4NFWcte20	0.035	0.832	0.252	0.099	-0.017	0
14	4NFWlin20	0.020	0.168	0.270	0.087	0.041	0
15	4NFWquad20	0.016	0.125	0.336	0.110	-0.0034	0
16	4NFWtuc20	0.015	0.117	0.278	0.036	-0.0044	0
17	1NFWcte30	0.071	6.965	0.273	0.259	-0.020	2
18	1NFWlin30	0.038	1.168	0.273	0.144	-0.010	0
19	1NFWquad30	0.039	0.208	0.284	0.156	0.012	0
20	1NFWtuc30	0.029	0.164	0.282	0.139	0.017	0
21	2NFWcte30	0.055	4.257	0.348	0.126	0.0063	1
22	2NFWlin30	0.019	0.201	0.177	0.144	0.012	0
23	2NFWquad30	0.016	0.088	0.252	0.059	0.015	0
24	2NFWtuc30	0.018	0.140	0.336	0.118	-0.0035	0
25	3NFWcte30	0.061	3.301	0.201	0.208	-0.034	1
26	3NFWlin30	0.045	0.585	0.282	0.069	0.141	0
27	3NFWquad30	0.031	0.240	0.202	0.096	0.059	0
28	3NFWtuc30	0.032	0.202	0.197	0.039	-0.018	0
29	4NFWcte30	0.053	4.438	0.350	0.082	0.052	3
30	4NFWlin30	0.021	0.400	0.332	0.031	-0.025	1
31	4NFWquad30	0.018	0.097	0.248	0.141	0.014	0
32	4NFWtuc30	0.017	0.106	0.256	0.054	0.039	0

Table 4.6: Shape parameters for simulations following a Plummer distribution for the DM halo.

N°	Simulation	C	Σ_C $[\frac{M_\odot}{pc^2}]$	Asymmetry	e	A_4	Surv SC(s)
33	1Plcte20	0.107	2.632	0.469	0.540	0.103	2
34	1Pllin20	0.058	0.721	0.334	0.160	0.049	0
35	1Plquad20	0.038	0.501	0.257	0.683	0.034	0
36	1Pltuc20	0.060	1.201	0.212	0.469	-0.058	1
37	2Plcte20	0.126	1.864	0.305	0.283	-0.005	2
38	2Pllin20	0.059	0.299	0.289	0.253	0.098	1
39	2Plquad20	0.057	0.837	0.454	0.322	0.037	1
40	2Pltuc20	0.071	1.535	0.235	0.317	-0.068	1
41	3Plcte20	0.112	0.717	0.441	0.449	-0.103	0
42	3Pllin20	0.069	0.322	0.429	0.453	0.056	0
43	3Plquad20	0.065	0.177	0.234	0.418	-0.115	0
44	3Pltuc20	0.096	0.216	0.241	0.493 -	0.023	0
45	4Plcte20	0.082	0.633	0.306	0.197	-0.024	1
46	4Pllin20	0.078	0.958	0.269	0.322	-0.125	0
47	4Plquad20	0.054	0.266	0.234	0.330	-0.0316	0
48	4Pltuc20	0.052	0.204	0.157	0.282	0.008	0
49	1Plcte30	0.183	4.149	0.518	0.052	-0.034	12
50	1Pllin30	0.128	3.901	0.309	0.386	-0.088	9
51	1Plquad30	0.132	4.147	0.371	0.339	-0.062	9
52	1Pltuc30	0.122	3.636	0.424	0.164	-0.152	9
53	2Plcte30	0.186	4.911	0.538	0.099	-0.004	13
54	2Pllin30	0.171	4.984	0.473	0.196	0.003	11
55	2Plquad30	0.119	4.565	0.395	0.178	0.113	10
56	2Pltuc30	0.136	5.713	0.386	0.220	-0.00161	9
57	3Plcte30	0.330	6.553	0.509	0.155	0.005	9
58	3Pllin30	0.128	4.361	0.373	0.184	0.108	6
59	3Plquad30	0.102	3.469	0.257	0.538	-0.178	5
60	3Pltuc30	0.293	3.874	0.616	0.185	-0.002	7
61	4Plcte30	0.154	3.61	0.451	0.283	-0.074	6
62	4Pllin30	0.120	3.589	0.358	0.310	-0.023	5
63	4Plquad30	0.089	4.576	0.247	0.299	-0.032	5
64	4Pltuc30	0.179	5.165	0.341	0.195	0.031	5

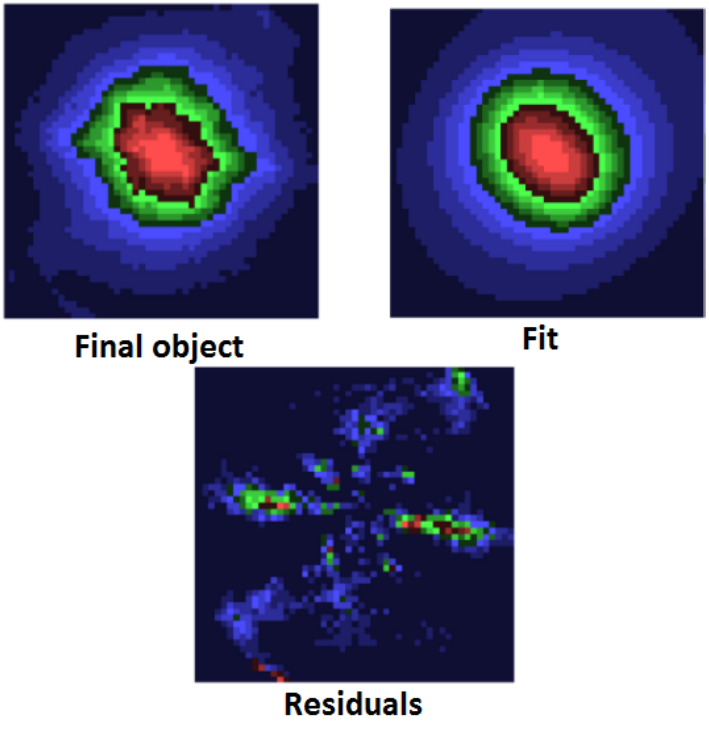

Figure 4.3: IRAF snapshot of our model. The left panel show the original simulation data in a radius of 500pc, the right panel the smooth model fitted to the data using ELLIPSE task from IRAF and finally the bottom panel shows the positive residuals, if we subtract the smooth model from original data.

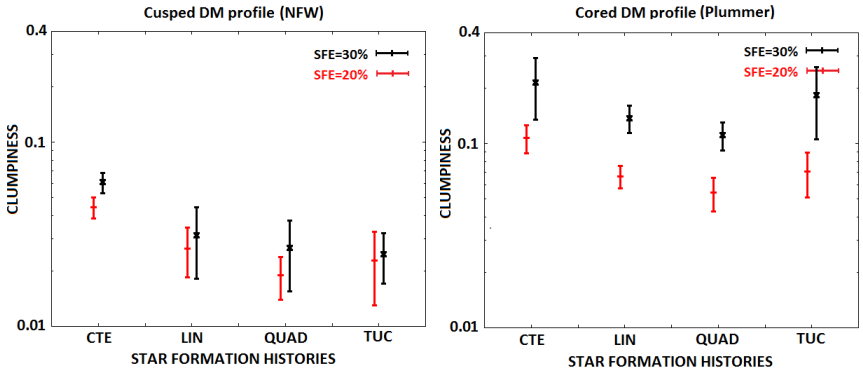

Figure 4.4: Mean clumpiness values for different SFHs and SFEs in a cusped DM halo (left panel) and a cored DM halo (right panel). Simulations with SFE=30% are shown in black and SFE=20% is denoted by red symbols. Note, that the y-axis has a logarithmic scale. Cored DM halo models have higher clumpiness values than cusped models, furthermore recent star formation and higher SFE give us more inhomogeneous final objects.

First, we observe that all our simulations lead to low values of the clumpiness parameter. This is a hint that the substructure we see in the brightness maps of our model might be only visible due to our larger than reality particle resolution. But those faint structures in our simulations are definitely real and not due to noise and the brighter ones should be observable.

These plots show that models with recent star formations have higher values of clumpiness than models without. The later the star clusters form the less time they have to be dissolved and form a homogeneous final object. Furthermore, the value of clumpiness depends on the SFE: If the SFE is higher (30%) the star clusters will need more time to dissolve after gas-expulsion leading to higher values of clumpiness than models with low SFE (20%).

Furthermore, the value of clumpiness will depend on the SFE: If the SFE is higher (30%) the star clusters will need more time to be dissolved

after the gas expulsion and this will lead to higher values of clumpiness than models with low SFE (20%).

We observe that in a cored DM profile we measure higher clumpiness parameters than in cusped models. This is a consequence that Plummer models have central crossing times larger than models with NFW profile and less interaction time to erase substructure. Also a cusp is more efficient in dispersing stars from their original orbits, leading to a more homogeneous distribution with time.

The larger error bars in the clumpiness value for cored DM halo and SFE=30% are due to the high number of surviving SCs, so our final object is not easy to fit with those substructures in the image.

It is hard to compare our results with the classical dSph of the MW as there was not yet a determination of their clumpiness published, but we observe in classical dSph elongations, twists, deviations from ellipses and/or double cores that are also visible in our models, see Figure 4.5.

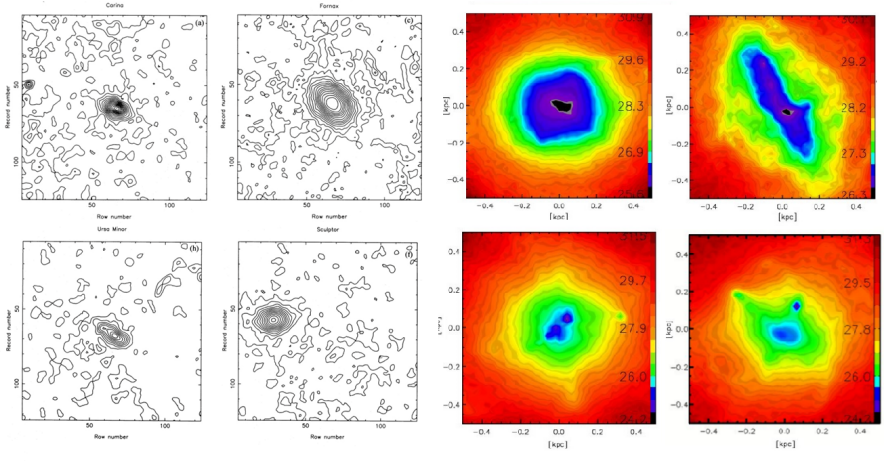

Figure 4.5: Comparison between real data and our simulations: Left side show four classical dSph galaxies (Carina, Fornax, Ursa minor and Sculptor) in which we can see twisted contours, deviations from ellipses and/or double cores (contour image taken from Irwin 1995). The left side show our final objects.

4.2.2 Surface density of clumpy substructures

As we show before, models with a recent star formation generate final objects with more substructure. In this subsection we will see that those substructures have higher surface density, Σ_c.

The Σ_c parameter is not an absolute value, because it corresponds to a difference between the Σ_0 of the final object and the surface density obtained from ELLIPSE routine parameters fit Σ_{ell}. Σ_c is measured in one pixel of 20pc of the residual image and does not correspond to the sum of all clumpy pixels. The presence of surviving SCs in our final objects will give us higher values of the Σ_c parameter.

In Figure 4.6 we compare the models with different DM halos, cored and cusped, we see that the cored models have higher values of Σ_c than cusped models, in models with recent star formation these values are higher due to the SCs which are not dissolved, also a high SFE=30% will give us clumps with values higher than models with a SFE=20%.

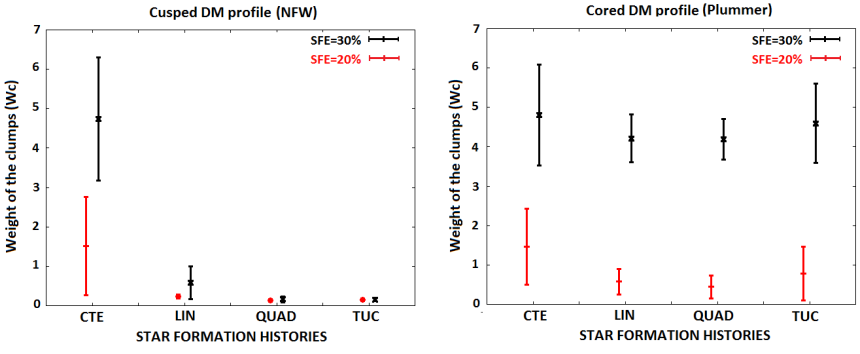

Figure 4.6: Weight of the clumps of our final objects versus the SFH, red color is for models with SFE=20% and black is for models with SFE=30%, left panel is for cusped DM halo and right panel for cored DM halo, we see that models with recent star formation have higher values for the weight of the clumps, this is due to the presence of surviving SCs mainly.

In general, models with a NFW profile for the DM halo and no recent star formation generate final objects where the surface brightness of the clumpy substructures is lower than models with Plummer profiles and relatively close to the brightness limit that a telescope can detect (Majewski et al 2005).

4.2.3 Ellipticity

Another structural parameter is the ellipticity, ϵ. This parameter is defined by

$$\epsilon = 1 - \frac{b}{a} \tag{4.5}$$

Where b is the minor axis and a is the major axis of an ellipse. The ellipticity values for some dSph of the Local Group are for example, Sculptor 0.32 $\pm$ 0.03, Fornax 0.31 $\pm$ 0.03, Ursa Minor 0.56 $\pm$ 0.05 and Draco 0.29 $\pm$ 0.01 according to Mateo M. 1998

The parameter ϵ is obtained from the ELLIPSE routine, this routine give us a ellipticity value at different radius for each isophote, we analyze the ellipticity value for the isophote at a radius of 500 pc in our results.

In Figure 4.7 we observe that the final object in our simulations have ϵ values close to the values of the classical dSph galaxies. We obtain different values from 0.03 until 0.6, which is in agreement with observations. This result is interesting, given the fact that we always start our simulations with a spherical distribution of star clusters. Also we find that cored simulations give us higher values of ellipticity than cusped simulations, There is no physics reason behind this result and is due only by chance because several star cluster have a similar orbit in the center of the DM halo and they dispersed its stars around this orbit.

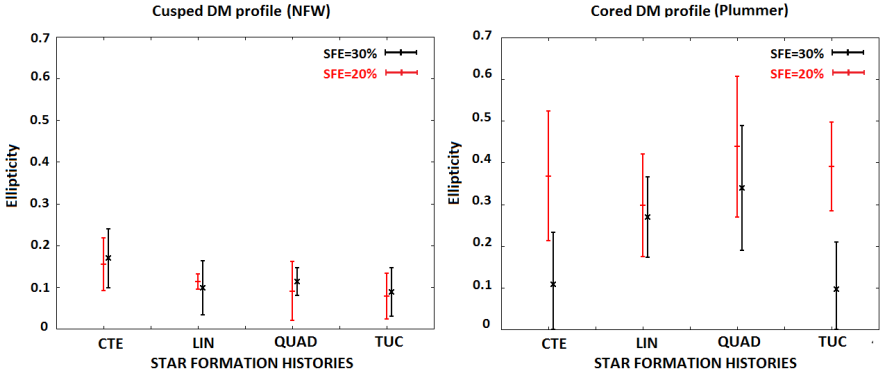

Figure 4.7: Ellipticity values of our final objects versus the SFH, red color is for models with SFE=20% and black is for models with SFE=30%, left panel is for cusped DM halo and right panel for cored DM halo, we see that ellipticity values are in the range of ellipticity observed in classical dSph, also we see that models with a cored DM halo give us higher values of ellipticity, but this result is given by chance.

4.2.4 A_4 isophotal parameter

Another parameter that can be obtained from the ELLIPSE routine is the fourth-order coefficient, A_4, which is the result of a Fourier analysis. A_4 corresponds to the value of the isophotal deviation from a perfect ellipse. A_4 is positive when one is dealing with "disky" galaxies. In contrast, negative values characterize "boxy" galaxies (Khochfar et al. 2005).

In Figure 4.8 We show that there is no observable trend between A_4 or any of our conditions and also A_4 tends to zero, this shows the spheroidal character of the resulting objects of our simulation.

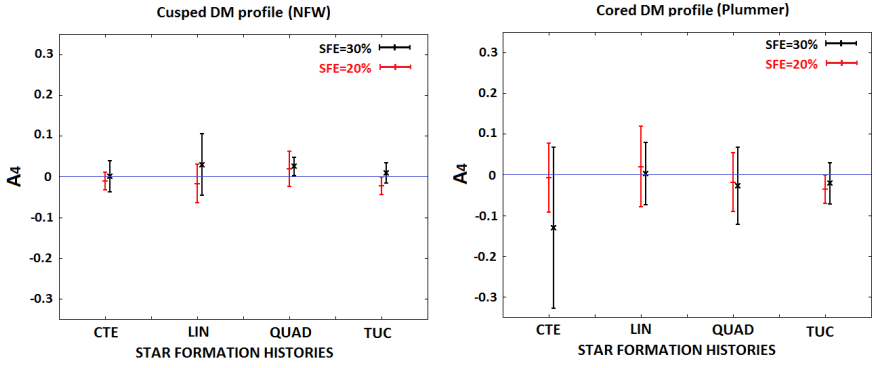

Figure 4.8: A_4 isophotal parameter: A_4 values of our final objects versus the SFH, red color is for models with SFE=20% and black is for models with SFE=30%, left panel is for cusped DM halo and right panel for cored DM halo, we show that there is no observable trend between A_4 or any of our conditions and also A_4 tends to zero, this shows the spheroidal character of the resulting objects of our simulation.

4.2.5 Asymmetry

The asymmetry index (Conselice et al. 2003), has been used previously to quantify the morphologies of galaxies.

To calculate this we rotate the image of our final object 180° and subtract this from the original image, then we calculate the absolute value of this subtraction and we sum all the pixel of this image, then the result is divided for the value of the original image and we obtain the asymmetry value, as is shown in Equation 4.6, in Figure 4.9 we show the process to calculate the asymmetry value with a graphic example.

$$\text{Asymmetry} = \frac{|\text{I} - \text{R}|}{\text{I}} \tag{4.6}$$

Where I is the original image and R is the original image rotated 180°.

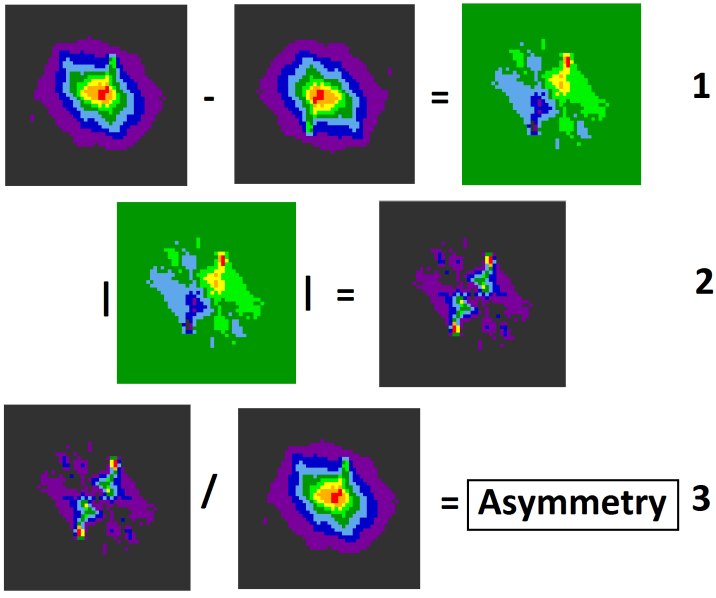

Figure 4.9: Calculating the Asymmetry of a final object: First we rotate the original image by 180° then we subtract them as is shown in (1), then we calculate the absolute value as is shown in (2) and finally we divide the sum of all the pixel of the image obtained in (2) by the sum of all the pixel of the original image in (3).

Figure 4.10 show that cored DM models give us final objects which are more asymmetric than cusped models due to the presence of surviving SCs mainly. Also we see a slight trend between the SFH and the asymmetry in cored simulations and in models with a cusped profile and SFE=30%, in both cases, models with recent star formation give us final objects with high asymmetry values.

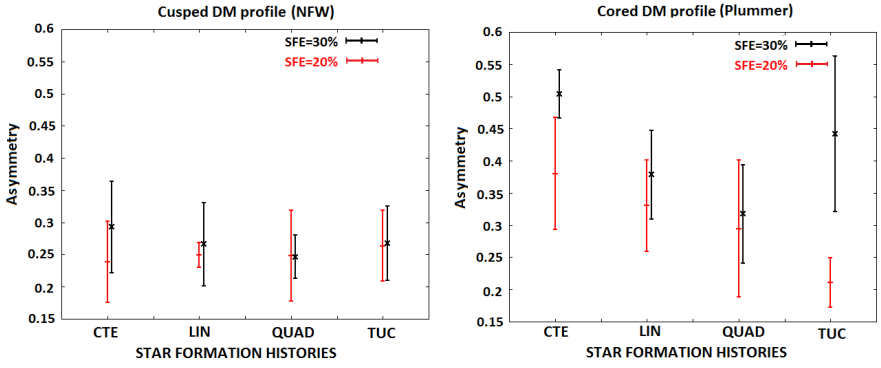

Figure 4.10: Asymmetry values of our final objects versus the SFH, red color is for models with SFE=20% and black is for models with SFE=30%, left panel is for cusped DM halo and right panel for cored DM halo, these plots show that there is a slightly correlation between the SFH and the asymmetry, models with recent star formation give us higher values of asymmetry, because the SCs need more time to dissolve and form a symmetric final object.

4.2.6 Surviving SCs

Some of our final objects have several surviving SCs which are orbiting the center of the DM halo as shown in the left panel of Figure 2.d, those SCs can survive either because they need more time to get dissolved or because its orbit is very close to the center of the DM halo, then some stars can not scape from the SC, they are captured again and the SC can not be dissolved easily, we consider a SCs to be dissolved if it has less than 10% of particles left bound. In Figure 4.11 we see the correlation between the number of surviving SCs and the SFH, SFE and DM profile.

We show that in simulations with low SFE (20%) there are no surviving SCs in cusped DM halo, because they need just a few hundred Myr to get dissolved, on the other hand, in simulations with cored DM profiles the number of surviving SCs increases in models with a constant SFH because some of the latest SCs formed will need more time than

the duration of the simulation to be dissolved. Also in the second set of initial condition the latest star cluster was not dissolved in each SFH because its orbit have a apogalactic distance very close to the center of the DM halo and it is hard to dissolve a SCs with that feature as we will show in the next subsection.

In simulations with high SFE (30%), the number of surviving SCs is a bit higher for cusped DM profile, because we need approximately 1 Gyr or less to dissolve the SCs, on the other hand for cored DM profiles the number of surviving SCs is higher, and there are some star cluster which can not be dissolved even after 10 Gyr if the apogalactic distance is small (< 300 pc), in Figure 4.12 we show the process of dissolution of a SC orbiting the center of a DM halo, we see this SC is expanding while is orbiting the center of the DM halo, it expands when pass near to the center and collapse while it goes far from the center.

Intuitively, we have more surviving SC in simulations with recent star formation because the latests SCs which are placed within the DM halo have less time to be erased completely in comparison to the older SCs.

Dissolving time of SCs

The time to erase a SC will vary depending on its orbit, SFE and the DM profile, in Figure 4.13 we plot the correlation between the dissolving time and the apogalactic distance for both DM halos and SFE, top panels are for models with a SFE=20% and bottom panels for SFE=30%, left panels are for a cusped models and right panels for cored DM simulations. In order to say that a SC is dissolved we measure the time when less than 10% of the particles are bound.

Figure 4.13 shows that for cusped DM profile the dissolving time is lower and will not take more than 1 Gyr to dissolve a single SC even if the SFE is high (30%). On the other hand for cored DM profiles and SFE=20% the dissolution time is higher (> 1 Gyr) if the apogalactic distance of the orbit is small (< 300 pc) , this is due because the stars of the SC can not escape easily from the potential well of the cored DM halo and after one crossing time the stars are captured again by the SC, the same will happen if we increase the SFE to 30%, but now the SCs

with smallest orbit will need more than 10 Gyr to get dissolved.

The presence of surviving SCs in our simulations, could give us predictions for future observations to corroborate our formation scenario, for example Sagittarius have one globular cluster and in Fornax there are five old SCs discovered orbiting this galaxy and in several dwarf galaxies we see young star clusters (grasha et al.2017).

Some authors claim that the stellar substructures seen in Fornax are the result of a past merger (Coleman et al. 2004; Coleman & Da Costa 2005; Amorisco & Evans 2012; Yozin & Bekki 2012; del Pino et al. 2015). On the other hand, de Boer et al. (2013) claim that these clumps are more likely the result of a quiet infall of gas previously expelled from Fornax during its star formation episodes.

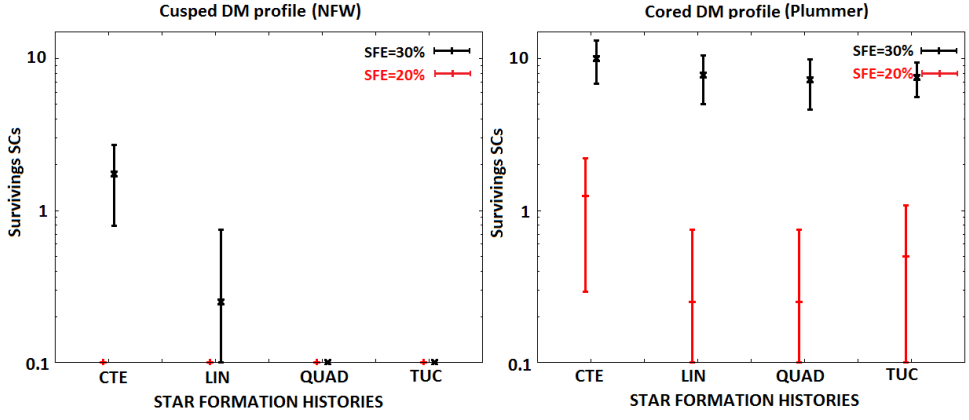

Figure 4.11: Number of surviving SCs vs. SFH; the left panel are simulations with a cusped DM halo profile, the right panel are the simulations with a cored DM profile. Red symbols denote SFE=20% and black SFE=30%. The y-axis has a logarithmic scale and therefore 0 surviving SCs are marked as 0.1 in the plots. In cusped DM halos the SCs dissolve easily and we do not see any of them in simulations with no recent star formation. In cored DM halos we will have several surviving star clusters even with a SFE=20% and no recent star formation.

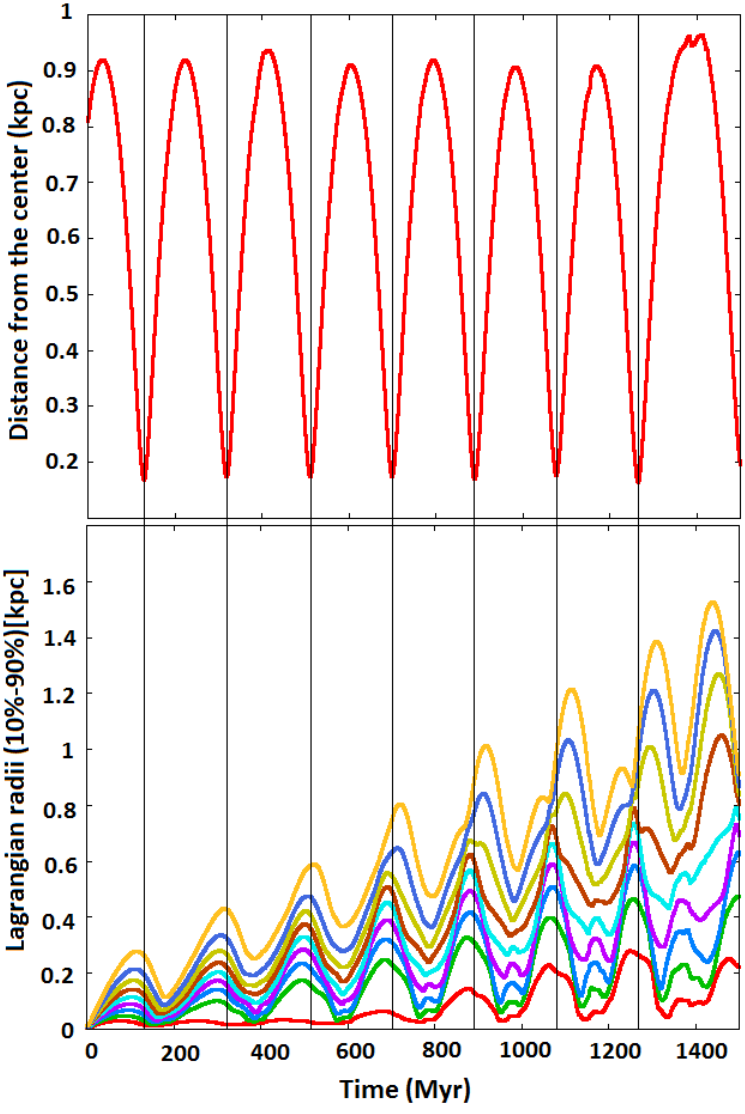

Figure 4.12: This plots are taken from a SC in a cored DM halo and a SFE=30%. The top panel is the orbit of a single SC orbiting the center of the DM halo and the bottom panel Lagrangian radii (10%-90%), we see that the SCs is expanding and collapsing while is orbiting the DM halo, the SC expand while is passing near to the center and collapse when it go far of the center of DM halo.

As a general conclusion for this section our models with a low SFE=20% and a DM halo with a NFW profile, the SCs can be dissolved in less than 300 Myr, so we can resemble the properties of a classical dSph even if we have recent star formation histories. Models with a cored DM halo following a Plummer sphere profile, need more time to dissolve the SCs ($\approx$500 Myr), and if the apogalactic distance of these SCs is near to the center of the DM halo (< 400 pc), they will need approximately 2 Gyr to get dissolved, so we can resemble the properties of a classical dSph only if we have no recent star formation in the galaxy in cored simulations and SFE=20%.

In our models with SCs with a high SFE=30% and a DM halo following a NFW profile, the SCs need approximately between 300 Myr to 1 Gyr to get dissolved, and again as we do not see surviving SCs in classical dSph, we can say that our models with cusped DM profile and SFE=30%, work only if we do not have recent star formation history in the galaxy. On the other hand, models with a cored DM profile and SCs with a SFE=30%, can not resemble the properties of classical dSphs, because some of the SCs can not be dissolved if their apogalactic distance is close to the center of the DM halo, they could need more than 10 Gyr to be dissolved, but this could be a hint to explain the formation of the Fornax galaxy which is a dSph galaxy with 5 SCs orbiting its center.

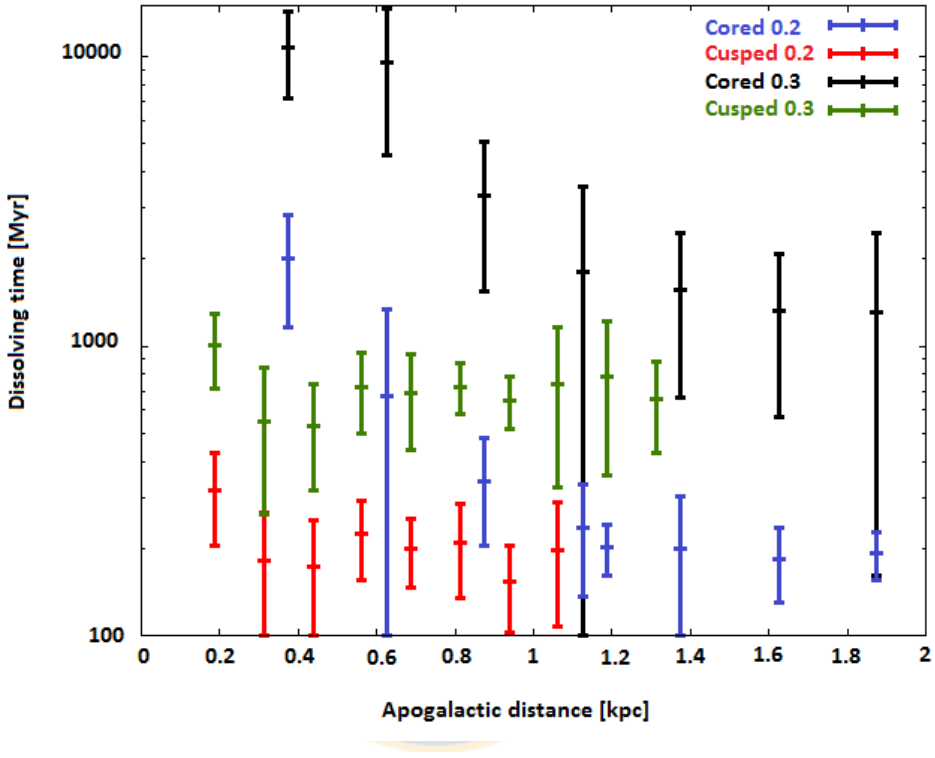

Figure 4.13: Dissolution time vs. apogalactic distance: This plot shows the dissolution time of the star clusters according to their orbit, dark matter profile of the halo and SFE. Blue is for cored DM halos and a SFE of 0.2, red is for cusped and 0.2, black for cored and 0.3 and finally green is for cusped and 0.3. We can see that the dissolution time is always larger for cored than for cusped halos and larger for higher SFEs. Furthermore, we see a clear trend that SCs orbiting closer to the center (small apo-galacticons) have significantly larger dissolution times in the cored simulations.

4.3 Velocity space

4.3.1 Velocity dispersion

The dSph satellite galaxies of the MW are close enough to obtain high resolution measurements, resolving the line of sight velocity dispersion of 5 to 10 km/s (Walker G. et al. 2007).

We compare the line of sight velocity dispersion profile of the final objects with the typical velocity dispersion observed in classical dSph galaxies.

In the right panel of Figure 4.1, we show the line of sight velocity dispersion profiles for some of our simulations. These profiles have been obtained considering the mean value of the line of sight velocity dispersion of pixels within a concentric ring with a varying radius. In all the simulations the velocity dispersion profiles obtained are always more or less flat, except in models with a high quantity of surviving SCs like Figure 4.1(d), all of our models show velocity dispersions in the range of 5-12 km/s, which agrees with observations (see Figure 4.14) and the previous work (Assmann et.al 2013b), see Figure 4.15.

Looking at the outer part of the profiles we observe different types of behavior in the velocity dispersion. We get outer profiles (beyond 1kpc) where the velocity dispersion falls slowly in some cases, while in others the dispersion stays flat. We see a similar behavior in the MW's dwarf galaxies. In Sextans we see a slight drop in velocity dispersion around 1 kpc, while Sculptor, Draco and Fornax show flat profiles (see Figure 4.14 taken from Walker G. et al. 2007).

The inner part some of our simulations show wiggles and bumps in the velocity dispersion profile. While the observers always try to fit smooth curves, thus implicitly assuming that any bumps seen in the profiles are merely due to statistical noise, (e.g. Sculptor, Draco or Carina) in our models, the strange bumps in the observed profiles may not be simply due to noise in the observed data sets. According to our formation theory they are a natural product of the formation scenario proposed.

These results show clearly that our models are well suited to reproduce the formation of dSph galaxies. We can show that we can reproduce the dynamics of the different dwarf galaxies with our models.

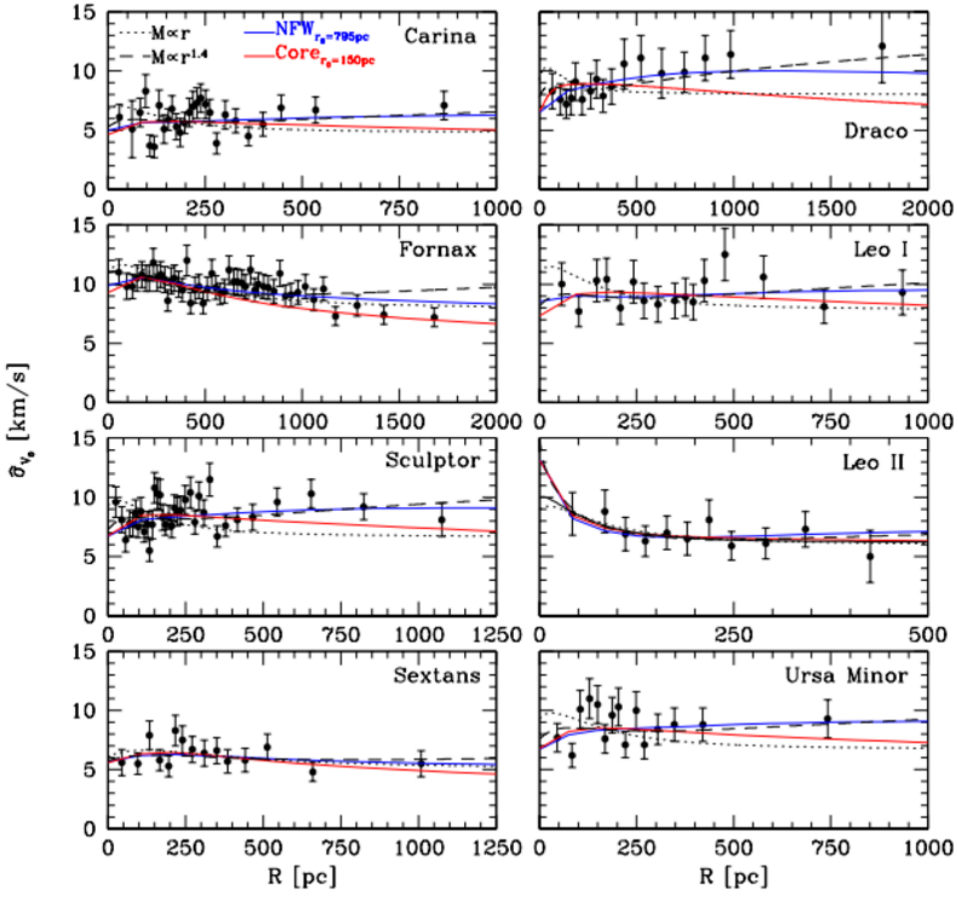

Figure 4.14: Velocity dispersion profile observed in some classical dSph galaxies, we observe velocities in the range of 5-12 km/s, the measurement have larger error bars which are fitted with a line, in our models those wiggles and bumps are real and not due to noise.

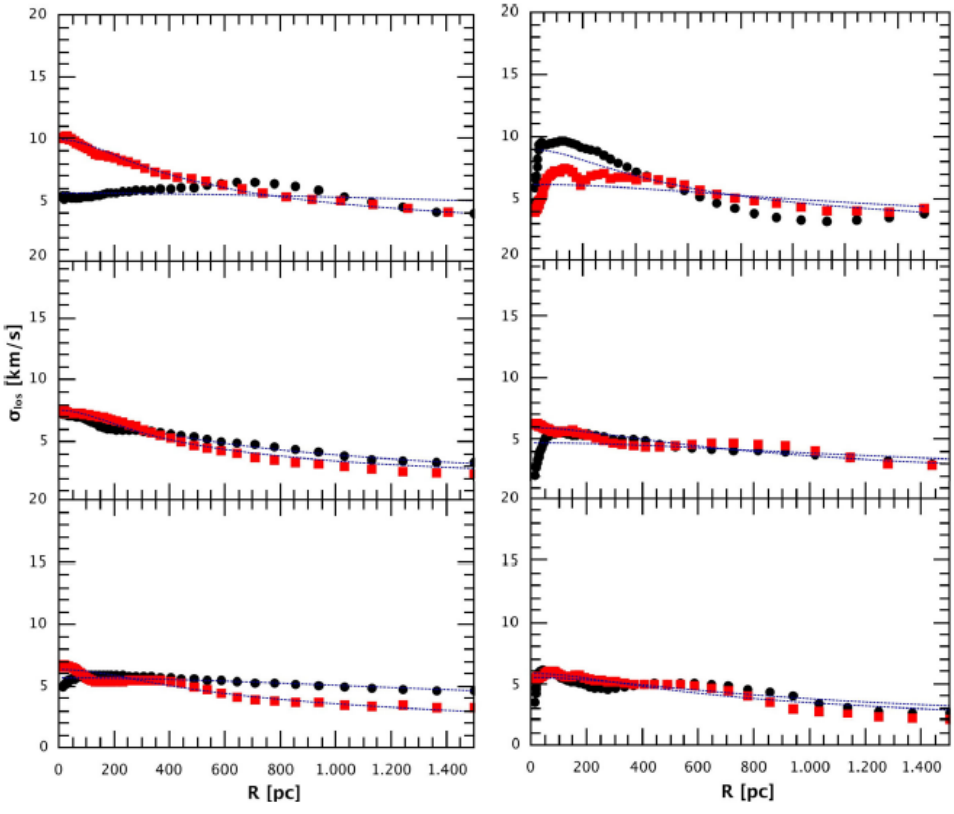

Figure 4.15: Assmann et al. (2013) velocity dispersion plots: Line of sight velocity dispersion profile for cusped (left-hand panels) and cored (right-hand panels) DM haloes for simulations with $M_{500}=10^7 M_\odot$. From top to bottom, the scale lengths of the DM halo are 1.0, 0.5 and 0.25 kpc, respectively. Black and red colors correspond to simulations which initially have 15 or 30 SCs. Dashed lines are the fitting curves given by a Plummer fit to the data. For both types of DM haloes, the velocity dispersion profiles obtained are always more or less flat, out to large radii, as seen with dSph galaxies

Chapter 5

Discussion and Conclusions

Our simulations can resemble the observed properties of classical dSph, as for example an exponential surface brightness profile and a flat velocity dispersion in the range of 5 to 12 $\mathrm{km\,s^{-1}}$. Furthermore, we can resemble specific properties seen in some dSph, as for example off-center nuclei (Sextans), secondary density peaks (Ursa Minor) or dents in the contours (Draco).

An important feature of our simulations is the presence or absence of surviving SCs. We identify three parameters which can be responsible for the survival of a star cluster. The most obvious one is a high SFE, which automatically leads to survival of the gas-expulsion phase. In our simulations, the SFEs used are below the threshold, which is usually believed to produce a surviving star cluster, even though 30% is close to the theoretical limit. Our simulations definitely show that lower SFEs lead to less or none surviving SCs. The next best reason should be that in the case of more recent SFH some SCs have not enough time to get completely dissolved. Again, we see this trend in our simulations. But, we identify a third possibility for SCs to survive and that is in the very center of a cored DM halo. A central core does not disperse the stars of the SC from their original orbit and so we see SC remnants, especially if the SC is close to its apo-centric distance. This might be a hint how to support the formation of nuclei in dwarf galaxies.

Our simulations provide a possible solution to why some dSph galaxies have orbiting star clusters and why some of them do not, and this

could be a hint to looking for faint surviving SCs in other dSph with the future telescopes. As the majority of dSph galaxies do not show associated SC, with the exception of Fornax and Sagittarius, we can deduce, that the SCs inside the DM halos have formed with low SFEs (¡ 30%) and most likely in a cusped DM profile as predicted by Λ-CDM.

The absence of surviving SCs in the observed dSph and the high presence of them in our cored simulations could be a hint for the solution of the cusp-core problem, which is a mismatch in the DM halo profiles between the prediction of cosmological Λ-CDM simulations, which say that the DM halo have to follow a cusped profile, and the observed kinematic data in dSphs which tell us that the DM profile is cored. In our models the SCs were dissolved more quickly in a cusped profile than in a cored DM halo, this could be a hint of the existence of a mechanism (e.g. feedback, modifications of the nature of dark matter) that eliminates the cusp in DM halos, as some authors claim (Governato F. et.al 2010).

Finally, we have to keep in mind that our models make a lot of simplifications, for example, we put the SCs in virial equilibrium within the DM halo for simplicity, because we do not know in which virial state the SCs are formed and also they follow a Plummer distribution because we expect to form more SCs in the center of the DM halo, also we assume that all the SCs have a Plummer sphere distribution, which is a good approximation to model a SC. Also all SCs have the same mass, we would expect that in dSphs with low star formation rate (SFR) we produce more and smaller SCs and with high SFR we would produce less and more massive SCs. Furthermore, objects with recent star formation are also the ones showing low SFRs and therefore the SCs would be easier to destroy. So we overestimate the number of surviving SCs in these simulations.

We assume the same SFE for each SC, and after the gas-expulsion the gas is lost to nowhere. This is justified because the mass of the gas is negligible with respect to the mass of the DM halo.

Another simplification of our models is that we use SUPERBOX, a particle mesh code which do not take in account two body interactions. It is useful in our case because a dSph galaxy is a collisionless system and the SCs are a collisional system only in their first 4 Myr before

gas-expulsion, so we can neglect these interactions.

Our previous models (Assmann et al. 2013a,b) were subject to questions, as we do not resemble any mass-metallicity relation found to be present in the dwarf galaxy population. As this is virtually impossible to include in a pure stellar dynamical simulation, we at least show with our new models that our previous results are not altered by including different observed SFHs. Still our models are purely stellar dynamics, but now one could include analytically ones favourite astro-chemical model to derive the yields for the later generations of SCs and paint the phase-space elements of our simulations according to their metal content.

In this Thesis we test a possible scenario for the formation of dSph galaxies proposed by Assmann et al. (2013a,b) and we add different SFHs to the numerical simulations. In our simulations we consider the evolution of 30 star clusters placed at different moments into our simulations to mimic the SFHs. The SCs are dissolving within a cored or a cusped dark matter halo. Also we study the effect of different SFEs (20% and 30%) for those SCs.

We observe that after 10 Gyr of evolution we get an object that resembles the properties of a classical dSph galaxy if we have enough time to dissolve the SCs.

In our models with a low SFE=20% and a DM halo with a NFW profile, the SCs can be dissolved in less than 300 Myr, so we can resemble the properties of a classical dSph even if we have recent star formation histories. Models with a cored DM halo following a Plummer sphere profile, need more time to dissolve the SCs ($\approx$ 500 Myr), and if the apogalactic distance of these SCs is near to the center of the DM halo ($<$ 300 pc), they will need approximately 2 Gyr to get dissolved. So we can resemble the properties of a classical dSph only if we have no recent star formation in the galaxy in cored haloes.

In our models with SCs with a high SFE=30% and a DM halo following a NFW profile, the SCs need approximately between 300 Myr to 1 Gyr to get dissolved, and again as we do not see surviving SCs in classical dSph, we can say that our models with cusped DM profile and SFE=30%, work only if we do not have recent star formation history in the galaxy. On the other hand, models with a cored DM profile and

SCs with a SFE=30%, can not resemble the properties of classical dSph, because some of the SCs can not get dissolved if their apo-galactic distance is close to the center of the DM halo, they need more than 10 Gyr to be dissolved, but this could be a hint to explain the formation of the Fornax galaxy which is a dSph galaxy with 5 SCs orbiting its center.

In all our models even if we have surviving SCs, we get surface brightness profiles as observed in classical dSph, we use a Sersic profile to fit the surface brightness profile of our final objects and we get effective radii similar to the observed in dSph with a mean value of 245 ± 26 pc for cusped and 523 ± 195 pc for cored profiles, also we get values of the n index close to unity ($n = 0.74 \pm 0.16$ for cusped and $n = 0.84 \pm 0.29$ for cored), this means that our final objects have exponential surface brightness profiles, as is observed in dSphs.

Furthermore, all our simulations show a velocity dispersion in the observed range of classical dSph, between 5-12 $\mathrm{km\,s^{-1}}$, and remain flat independent of the radius. Another important feature is that we see wiggles and bumps in the data. In observational papers these wiggles and bumps are smoothed over but according to our scenario some of them could be real. In reality we see similar bumps in Carina, Leo I and Sculptor (Walker et al. 2009).

Another important result is that our models give a hint to the cusp-core problem, as the SCs are more likely to get dissolved in a cusped DM halo, and observations shows that DM halos of dSph follow a cored profile. We suspect that there could be a mechanism that eliminates the cusp after the dissolution of the SCs and form a cored DM profile.

Our simulations show that our formation scenario works even if using different SFHs, DM halo profiles and low SFH to dissolve the SCs and we are not only able to reproduce the observational data that we have today, but provide observers with predictions for future observations.

Bibliography

Aarseth S. J., Henon M., Wielen R., 1974, A&A, 37, 183
Amorisco N.C., Evans N.W., 2012, ApJ, 756, L2
Assmann P., Fellhauer M., Wilkinson M.I., Smith R., 2013, MNRAS, 432,274
Belokurov V. et al., 2007, ApJ, 654, 897
Boily C. M., Kroupa P., 2003a, MNRAS, 338, 665
Boily C. M., Kroupa P., 2003b, MNRAS, 338, 673
Bonnell I. A., Smith R. J., Clark P. C., Bate M. R., 2011, MNRAS, 410, 2339
Bressert E. et al., 2010, MNRAS, 409, L54
Caon N., Capaccioli M., D'Onofrio M., 1993, MNRAS, 265, 10132
Cole, S.; Aragon-Salamanca, A.; Frenk, C. S.; Navarro, J. F.; Zepf, S. E. 1994, MNRAS, 271,781C
Coleman M., Da Costa G. S., Bland-Hawthorn J., Martínez-Delgado D., Freeman K.C., Malin D., 2004, AJ, 127, 832
Coleman M., Da Costa G. S., 2005, PASA, 22, 162
Conselice C. J., 2003, ApJS, 147, 1C
Dehnen W., McLaughlin D. E., 2005, MNRAS, 363, 1057
de Boer T. J. L., Tolstoy E., Saha A., Olszewski E. W., 2013, A&A, 551, A103
del Pino A., Aparicio A., Hidalgo S.L., 2015, MNRAS, 454, 3996
D'Onghia E., Besla G., Cox T., Hernquist L., 2009, Nat, 460, 605
Fellhauer M., Kroupa P., Baumgardt H., Bien R., Boily C. M., Spurzem R., Wassmer N., 2000, New Astron., 5, 305
Flaugher B., 2005, International Journal of Modern Physics A, 20, 3121

Gnedin O. Y., Hernquist L., Ostriker J. P., 1999, ApJ, 514, 109
Goodwin S. P., 1997a, MNRAS, 284, 785
Goodwin S. P., 1997b, MNRAS, 286, 669
Governato, F.; Brook, C.; Mayer, L.; Brooks, A.,Rhee, G.; Jonsson, P.; Willman, B.; Stinson, G.; Quinn, T.; Madau, P, 2010. Nature. 463: 203–206
K. Grasha, D. Calzetti, A. Adamo, H. Kim, B.G. Elmegreen, D.A. Gouliermis, D.A. Dale, M. Fumagalli, E.K. Grebel, K.E. Johnson, L. Kahre, R.C. Kennicutt, M. Messa, A. Pellerin, J.E. Ryon, L.J. Smith, F. Shabani, D. Thilker, L. Ubeda, 2017, arXiv, 1704, 06321
Irwin M., Hatzidimitriou D., 1995, MNRAS, 277, 1354
Jerjen H., Binggeli B., Freeman K. C., 2000, AJ, 119, 593
Kaiser N., et al., 2002, Survey and Other Telescope Technologies and Discoveries, Edited by Tyson, 4836, 154 Kauffmann G.,White S., Guiderdoni B., 1993, MNRAS, 264,201
King I. 1962, AJ, 67, 471
Kleyna J. T., Wilkinson M. I., Evans N. W., Gilmore G., Frayn C., 2002, MNRAS, 330, 792
Kleyna J. T., Wilkinson M. I., Gilmore G., Evans N. W., 2003, ApJ, 588, L21
Kleyna J. T., Wilkinson M. I., Evans N. W., Gilmore G., 2004, MNRAS, 354, L66
Klyrin, Anatoly, Kravtsov, 1999, APJ, 522
Koch A. et al., 2009, ApJ, 690, 453
Lada C. J., Lada E. A., 2003, ARA&A, 41, 57
Lada C. J., Lombardi M., Alves J. F., 2010, ApJ, 724, 687
Lokas E. L., 2009, MNRAS, 394, L102
Mayer L., Kazantzidis S., Mastropiero C., Wadsley J., 2007, Nat, 445, 738
Mateo M. L., 1998, ARA&A, 36, 435
Majewski S., Frinchaboy P.M., Kunkel W.E., 2005, AJ, 130,2677
Munoz R. R. et al., 2005, ApJ, 631, L137
Munoz R. R. et al., 2006, ApJ, 649, 201
Navarro J. F., Frank C. S., White S. D. M., 1997, ApJ, 490, 493
Parmentier G., Goodwin S. P., Kroupa P., Baumgardt H., 2008, ApJ, 678,347

Plummer H. C., 1911, MNRAS, 71, 460
Press W. et al., editors. Numerical Recipes. Cambridge University Press, Cambridge, UK, 1985.
Simon J. D., Geha M., 2007, ApJ, 670, 313
Smith R., Slater R., Fellhauer M., Goodwin S. P., Assmann P., 2011a, MNRAS, 416, 383
Smith R., Fellhauer M., Goodwin S. P., Assmann P., 2011b, MNRAS, 414, 3036
Walker M. G., Mateo M., Olszewski E. W., Gnedin O. Y., Wang X., Bodhisattva S., Woodroofe M., 2007, ApJ, 667, L53
Walcher C. J., Fried J. W., Burkert A., Klessen R. S., 2003, A&A, 406, 847
Walker M. G., Mateo M., Olszewski E. W., Penarrubia J., Evans N. W., Gilmore G., 2009, ApJ, 704, 1274
Walker M. G., Mateo M., Olszewski E. W., Gnedin O. Y., Wang X., Bodhisattva S., Woodroofe M., 2007, ApJ, 667, L53
Weisz, Daniel R.; Dolphin, Andrew E.; Skillman, Evan D.; Holtzman, Jon; Gilbert, Karoline M.; Dalcanton, Julianne J.; Williams, Benjamin F.2014, ApJ, 789, 147W
Whitmore B. C., Zhang Q., Leitherer C., Fall S. M., Schweizer F., Miller B.W., 1999, AJ, 118, 1551
York D. G., et al., 2000, AJ, 120, 1579
Yozin C., Bekki K., 2012, ApJ, 756, L18